

See discussions, stats, and author profiles for this publication at: <https://www.researchgate.net/publication/382798400>

# A Frequency-Based Hierarchy of Dynamical Models in Cislunar Space: Leveraging Periodically and Quasi-Periodically Perturbed Models


Preprint · August 2024

DOI: 10.21203/rs.3.rs-4822764/v1

CITATIONS  
2

READS  
203

3 authors:




Beom Park

Purdue University

12 PUBLICATIONS 63 CITATIONS

SEE PROFILE




Kathleen Howell

Purdue University

328 PUBLICATIONS 7,728 CITATIONS

SEE PROFILE



Rohith Reddy Sanaga

Purdue University

6 PUBLICATIONS 16 CITATIONS

SEE PROFILE

# A Frequency-Based Hierarchy of Dynamical Models in Cislunar Space: Leveraging Periodically and Quasi-Periodically Perturbed Models

Beom Park

[park1103@purdue.edu](mailto:park1103@purdue.edu)

Purdue University West Lafayette

Rohith Reddy Sanaga

Purdue University West Lafayette

Kathleen C. Howell

Purdue University West Lafayette

---

## Research Article

**Keywords:** CR3BP, QBCP, HR4BP, Model Fidelity

**Posted Date:** August 1st, 2024

**DOI:** <https://doi.org/10.21203/rs.3.rs-4822764/v1>

**License:**   This work is licensed under a Creative Commons Attribution 4.0 International License.

[Read Full License](#)

**Additional Declarations:** No competing interests reported.

---

# A Frequency-Based Hierarchy of Dynamical Models in Cislunar Space: Leveraging Periodically and Quasi-Periodically Perturbed Models

Beom Park<sup>1\*</sup>, Rohith Reddy Sanaga<sup>1</sup> and Kathleen C. Howell<sup>1</sup>

<sup>1</sup>School of Aeronautics and Astronautics, Purdue University, 610 Purdue Mall, West Lafayette, 47907, IN, U.S.

\*Corresponding author(s). E-mail(s): [park1103@purdue.edu](mailto:park1103@purdue.edu);  
Contributing authors: [rsanaga@purdue.edu](mailto:rsanaga@purdue.edu); [howell@purdue.edu](mailto:howell@purdue.edu);

## Abstract

Understanding the applicability of different dynamical models within cislunar space is a useful yet challenging problem. The current work constructs a hierarchy of dynamical models leveraging a common rotating reference frame that accommodates multiple dynamical models. In such a formulation, the Higher-Fidelity Ephemeris Model (HFEM) is approximated as quasi-periodically perturbed model with multiple frequencies in addition to the autonomous Circular Restricted Three-Body Problem (CR3BP) dynamics. Then, different intermediate models are evaluated within the hierarchy in terms of the types and numbers of the incorporated frequencies. The analysis focuses on three main topics. Firstly, coherent solar gravity modeling is properly defined with analytical and visual criteria that serve as useful metrics in assessing intermediate models. Secondly, two periodically perturbed models, i.e., Quasi Bi-Circular Problem (QBCP) and Hill Restricted Four-Body Problem (HR4BP), are investigated within the common rotating reference frame. The capabilities and limitations of these two models within the hierarchy between the CR3BP and HFEM are examined, focusing on the similarities and differences in the models. Thirdly, novel quasi-periodically perturbed models are introduced. Leveraging the insight from Hill's lunar theory, two models are designed denoted as In-plane Quasi-Hill Restricted Four-Body Problem (I-QHR4BP) and Out-of-plane Quasi-Hill Restricted Four-Body Problem (O-QHR4BP). These two models selectively introduce the eccentricity between the Earth-Moon system and the inclination of the lunar orbit with respect to the Earth ecliptic plane, respectively, in addition to the HR4BP. The global characteristics of these new models are analyzed within the common rotating reference frame. The capabilities of multiple models within

the model hierarchy are analyzed for two sample transition cases from the CR3BP to HFEM:  $L_2$  Lagrange point and the  $L_2$  9:2 synodic halo orbit.

**Keywords:** CR3BP, QBCP, HR4BP, Model Fidelity

## Glossaries

BCR4BP	=	Bi-Circular Restricted Four-Body Problem
CR3BP	=	Circular Restricted Three-Body Problem
ER3BP	=	Elliptic Restricted Three-Body Problem
HR3BP	=	Hill Restricted Three-Body Problem
HR4BP	=	Hill Restricted Four-Body Problem
I-QHR4BP	=	In-plane Quasi-Hill Restricted Four-Body Problem
HFEM	=	Higher-Fidelity Ephemeris Model
O-QHR4BP	=	Out-of-plane Quasi-Hill Restricted Four-Body Problem
PO	=	Periodic Orbit
QBCP	=	Quasi Bi-Circular Problem
QHR4BP	=	Quasi Hill Restricted Four-Body Problem
QPO	=	Quasi-Periodic Orbit

## 1 Introduction

Understanding the utility of different dynamical models within the field of astrodynamics is key in selecting a suitable model for a specific analysis. The fidelity of the model, i.e., the degree of exactness with reality, is one criterion to gauge the applicability of dynamical models. A lower-fidelity model, although relatively far from reality, incorporates key components from the dynamical environment in simplified forms. The simplification often leads to integrals of motion, Hamiltonian structures, and additional dynamical insights that all aid in the global characterization of the behavior of the artificial object of interest. A higher-fidelity model, in contrast, is perceived as closer to reality and the analysis derived from it is more likely to persist in actual flight. However, such a model often entails longer simulation times and challenges in identifying global patterns that facilitate the extrapolation of the analysis to different scenarios. While both lower- and higher-fidelity models are mutually complementary, for preliminary analysis, a lower-fidelity model offers significant benefits in generating intuition with efficient simulation processes.

Leveraging lower-fidelity models is potentially a non-trivial process in terms of (1) selecting a suitable lower-fidelity model for a given analysis and (2) transitioning the analysis to an appropriate higher-fidelity model. The process benefits from considering a “hierarchy” of dynamical models with respect to model fidelities. Starting from the simplest model possible, one that captures essential elements, the fidelity is gradually increased by introducing additional components until ultimately reaching the desired higher-fidelity model. Then, depending on the relative importance of the components,

different models within the hierarchy are deemed fit for the analysis and serve as suitable lower-fidelity models. A smooth transition also benefits from the hierarchy, where the results from lower-fidelity models are gradually refined by adding the complexities along the hierarchy.

The model hierarchy is expected to depend on multiple factors, including but not limited to, the spacecraft state and a particular epoch. Depending on these factors, different paths are constructed between the lower- and higher-fidelity models that potentially alter the hierarchy altogether. Thus, constructing a suitable hierarchy also encompasses understanding this natural complexity and dependency on the underlying factors. Within the Earth-dominated two-body dynamical regime, such dependencies are relatively well-understood. For instance, the relative magnitudes of perturbations originating from the Earth’s atmospheric drag, lunisolar perturbation, and Earth’s harmonics gravity up to different orders are well characterized, mainly as functions of the altitude from the Earth’s surface, e.g., in [Beutler \(2004\)](#). Thus, it is possible to selectively and gradually add these additional perturbations to a lower-fidelity model, e.g., the Earth two-body point-mass model, depending on the specific dynamical regime. For example, typically, for a very low-Earth orbit, incorporating the drag may be considered an immediate next step within the hierarchy as opposed to including lunar gravity.

Within cislunar space, the hierarchy of dynamical models remains elusive and is the focus of the current investigation. In the regions where both the Earth and the Moon exert non-negligible gravitational influence on the spacecraft, the Earth-Moon Circular Restricted Three-Body Problem (CR3BP) obviously emerges as an invaluable lower-fidelity model. This model supplies structures that are not available either in the Earth or Moon two-body models, such as Lagrange equilibrium points. The model is a time-independent Hamiltonian system that admits families of (quasi-) periodic orbits that aid in a more global characterization of the motion of spacecraft. However, constructing a suitable hierarchy from the CR3BP that successfully evolves to the Higher-Fidelity Ephemeris Model (HFEM) is challenging due to two key difficulties. Firstly, the CR3BP is often formulated within a nondimensional rotating frame that hinders direct comparison of acceleration magnitudes from the HFEM, often cast within an inertial frame. Thus, similar analysis as accomplished within the Earth-dominated two-body regime faces challenges. Secondly, force components that manifest “in addition” to those in the CR3BP are challenging to identify and may not be associated with clear, distinct sources. For example, while the Earth-Moon CR3BP assumes a constant distance between the Earth-Moon system, the HFEM supplies a complex Earth-Moon motion. This “pulsation” in the Earth-Moon distance originates from the mutual gravitational forces within the Sun-Earth-Moon system where both solar gravity and the lunar orbit eccentricity interact to vary the Earth-Moon distance; thus, it is challenging to pinpoint one physical source for pulsation.

One approach to construct a suitable hierarchy within cislunar space may be considered a “bottom-up” approach. In this strategy, intermediate models are defined by selectively introducing perturbations in addition to the CR3BP. These perturbations are in ideal forms that are designed to mirror *some* components of the HFEM. The models maintain favorable dynamical characteristics such as a Hamiltonian nature

and some periodicity in the perturbing accelerations, as typically represented in a rotating frame. For periodically perturbed models, notable options for intermediate models include the Elliptic Restricted Three-Body Problem (ER3BP), Bi-Circular Restricted Four-Body Problem (BCR4BP), Quasi Bi-Circular Problem (QBCP), and Hill Restricted Four-Body Problem (HR4BP), that introduce pulsation between the Earth-Moon system and/or solar gravity to the CR3BP. Multiple examples appear in literature that yield a quasi-periodically perturbed dynamical model as well (Assadian and Pourtakdoust, 2010; Villegas-Pinto et al., 2023; Kelly et al., 2023). In some cases, these different models are indeed capable of serving as suitable intermediaries between the CR3BP and the HFEM. However, *depending on multiple factors*, the most suitable model may vary, or, one idealized representation of a force component added to the CR3BP may be, in fact, altogether inappropriate; no single model always rises as the “best” intermediate model. Thus, an analytical criterion is required to understand these dependencies and more globally assess the capabilities of different intermediate models within the context of the model hierarchy.

A complementary, alternative approach for characterizing the hierarchy corresponds to a “top-down” strategy. Here, the gap between the HFEM and CR3BP is quantified first to inform the types of perturbations that need to be modeled in addition to the CR3BP. The first theoretical foundation for such a strategy is provided by Gómez et al. (2002), where an HFEM is represented as a variation of the CR3BP that involves time-dependent perturbations governed by five distinct frequencies within a common rotating frame. Thus, the intermediate models are viewed as incorporating  $n$  ( $1 \leq n \leq 4$ ) number of frequencies in addition to the CR3BP, filling in the gap between the lower- and higher-fidelity models by selectively introducing perturbations associated with the  $n$  selected frequencies. It is then possible to envision the hierarchy of models as in Fig. 1, where the fidelity increases generally by incorporating multiple perturbing frequencies as additions to the CR3BP. Some of these frequencies are associated with the anomalistic, synodic, and draconic lunar months, facilitating the recognition of perturbations with distinct origins and physical intuitions. Then, the updated formulation by Park and Howell (2024b) proposes a switch in the independent variables between the CR3BP and HFEM. Such a common formulation enables the separation and comparison of perturbing accelerations associated with distinct frequencies. In Park and Howell (2024b), the perturbing accelerations are first categorized into two dominant frequencies ( $\nu_{1,2}$ ) mainly associated with pulsation ( $\nu_1$ ) and solar gravity ( $\nu_2$ ). Then, the relative magnitudes of the perturbing accelerations are compared across cislunar space to aid in selecting suitable intermediate models along the hierarchy between the CR3BP and HFEM. In the work by Park and Howell (2024b), two intermediate models, ER3BP and BCR4BP, are examined as representative of modeling  $\nu_1$ - and  $\nu_2$ -perturbations, respectively. The capabilities and limitations of these models in introducing suitable perturbations are gauged in comparison to the HFEM.

## 1.1 Goals

The current investigation extends previous research efforts in constructing the hierarchy between the Earth-Moon CR3BP and the HFEM. The analysis leverages the

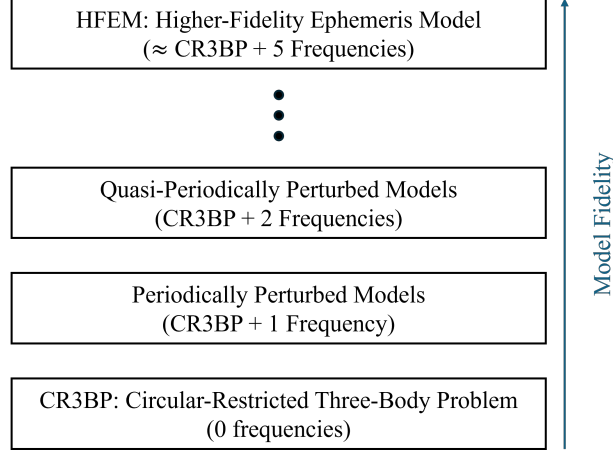


**Fig. 1:** Hierarchy of dynamical models in cislunar space leveraging frequencies

common formulation of equations originally proposed by Gómez et al. (2002) and adapted by Park and Howell (2024b) while focusing on following three key goals, (G1)-(G3):

- (G1) Introduce a proper definition for *coherent* solar gravity modeling: The coherency constitutes a key element in suitably adding the solar gravity to the CR3BP. Leveraging insights from Park and Howell (2023), analytical as well as visual criteria are introduced to properly assess the coherency of a given dynamical model that introduces the solar gravity in addition to the CR3BP.
- (G2) Catalog the QBCP and HR4BP within the common formulation: The *global* capabilities and limitations of the two periodically perturbed models with coherent solar gravity, i.e., the Quasi Bi-Circular Problem (QBCP) and the Hill Restricted Four-Body Problem (HR4BP), are assessed within the common formulation. This effort complements the previous “bottom-up” approaches that focus on specific regions within cislunar space, e.g., the vicinity of Lagrange points (Rosales et al., 2023; Peterson et al., 2023; Henry et al., 2023). In the current analysis, additional insights are provided regarding the similarities and differences between the QBCP and the HR4BP.
- (G3) Design coherent quasi-periodically perturbed models: Two quasi-periodically perturbed models are devised that maintain the coherent property for the solar gravity modeling. Leveraging previous insights from the Hill Restricted Three-Body Problem (HR3BP) and modern dynamical systems theory, the HR4BP (Scheeres, 1998) is extended to the In-plane Quasi-Hill Restricted Four-Body Problem (I-QHR4BP) and the Out-of-plane Quasi-Hill Restricted Four-Body Problem (O-QHR4BP). These two models introduce the lunar orbit eccentricity and inclination with respect to the Earth ecliptic plane, respectively, and serve as suitable “next steps” with two frequencies within the model hierarchy as illustrated in Fig. 1.

The investigation initially reviews the pulsating-rotating frame common formulation in Section 2. In Section 3, the coherent solar gravity is properly defined (G1). Then, two periodically perturbed models, the QBCP and HR4BP, are represented within the common formulation (G2), illustrating the differences and similarities of these models. In Section 4, two novel quasi-periodically perturbed models are introduced (G3), leveraging the quasi-periodic structures within the HR3BP. The equations of motion are provided in the common reference frame. The capabilities of multiple intermediate models within the hierarchy are assessed in terms of two sample transition scenarios from the Earth-Moon CR3BP structures to the HFEM counterparts in Section 5 for the  $L_2$  Lagrange point and the  $L_2$  9:2 synodic resonant halo orbit. Lastly, concluding remarks are provided in Section 6.

## 2 Review: Pulsating-Rotating Frame Coefficient Formulation

Frames and independent variables that are relevant to the current investigation are introduced, suited for different dynamical models. Then, a common formulation that accommodates multiple dynamical models, originally proposed by Gómez et al. (2002) and updated in Park and Howell (2024b), is reviewed.

### 2.1 Frame and Independent Variables

In the literature, various rotating frames are employed for deriving CR3BP as well as extensions to the CR3BP, e.g., HR4BP. The graphical illustrations and symbols for each frame under current investigation are included in Fig. 2 and Table 1, respectively. The Hill frame is a Sun-Earth rotating frame centered at the Earth, depicted in Fig. 2(a). The frame is leveraged to represent the lunar position vector with respect to the Earth, denoted as  $\vec{r}_{EM} = \xi \hat{i}_H + \eta \hat{j}_H + \zeta \hat{k}_H$ . Such a vector and the vector basis are leveraged for the HR3BP that aids in derivation of the HR4BP. Throughout the current investigation,  $(\vec{\cdot})$  symbolizes a vector and  $(\hat{\cdot})$  denotes a unit vector. The vector  $\vec{r}_{EM}$  adopts a nondimensional (nd) representation, where dimensional quantities are retrieved by multiplying  $l_H$ , defined as,

$$l_H = l_{SB*} \left( \frac{\tilde{\mu}_E + \tilde{\mu}_M}{\tilde{\mu}_S} \right)^{1/3}. \quad (1)$$

The distance between the Sun and the Earth-Moon barycenter ( $B$ ), assumed to be a fixed quantity in some models including the HR4BP, is symbolized by  $l_{SB*}$ . The  $\tilde{\mu}$  denotes the dimensional gravitational parameters for the celestial bodies with the subscripts  $E, M, S$  representing the Earth, Moon, and Sun, respectively. The unit vectors between the Hill frame and an inertial frame are related via the following rotation cosine matrix  $\mathbf{C}_H$  (matrix is in boldface),

$$\mathbf{C}_H = \begin{bmatrix} \cos m\tau & -\sin m\tau & 0 \\ \sin m\tau & \cos m\tau & 0 \\ 0 & 0 & 1 \end{bmatrix}, \quad (2)$$



where  $\tau$  corresponds to the Hill nd time. The parameter  $m \approx 0.0808$  is defined such that  $(1 + m)$  tracks the ratio of the synodic lunar month to the sidereal lunar month. Then, the relationship between the nd Hill frame position vector and the dimensional inertial frame vector is constructed as  $\vec{R}_{EM} = l_H \mathbf{C}_H \vec{r}_{EM}$ .

The uniform-rotating frame in Fig. 2(b) is formulated to describe the spacecraft (c) within the Earth-Moon system. The nd position vector for the spacecraft is denoted as  $\vec{\rho}_* = x_* \hat{x}_* + y_* \hat{y}_* + z_* \hat{z}_*$ , measured from the barycenter,  $B$ . A constant characteristic length  $l_*$  dimensionalizes the distance, corresponding to the average Earth-Moon distance. Then, the relationship between  $\vec{R}$ , the dimensional inertial position vector for the spacecraft, and  $\vec{\rho}_*$ , the nd position vector within the uniform-rotating frame, is constructed as  $\vec{R} = \vec{B} + l_* \mathbf{C}_* \vec{\rho}_*$ . The vector  $\vec{B}$  denotes the Earth-Moon barycenter position within the inertial frame. The direction cosine matrix is evaluated as,

$$\mathbf{C}_* = \begin{bmatrix} \cos t_* & -\sin t_* & 0 \\ \sin t_* & \cos t_* & 0 \\ 0 & 0 & 1 \end{bmatrix}, \quad (3)$$

where  $t_*$  is the uniform nd time. Within the uniform-rotating frame, the rotation rate for the frame is held constant at unity with respect to  $t_*$ , regardless of the actual motion of the Earth-Moon system. Thus, for the case where the dimensional Earth-Moon distance varies over time, the locations of the Earth and the Moon vary within the uniform-rotating frame as illustrated in Fig. 2(b). This frame is leveraged to describe the HR4BP dynamics as originally derived by Scheeres (1998).

The pulsating-rotating frame (Fig. 2(c)) depicts an alternative rotating frame for the Earth-Moon system, where the spacecraft nd position vector is represented as  $\vec{\rho} = x\hat{x} + y\hat{y} + z\hat{z}$ . While the origin of the frame is still at the Earth-Moon barycenter, the dimensionalization quantity varies to instantaneously mirror the varying Earth-Moon distance,  $l$ . Also, the direction cosine matrix is constructed as,

$$\mathbf{C} = [\hat{x} \ \hat{y} \ \hat{z}], \quad (4)$$

where  $\hat{x} = \vec{R}_{EM}/l$ ,  $\hat{z} = \vec{h}/h$ ,  $\hat{y} = \hat{z} \times \hat{x}$  define the columns. Here,  $\vec{R}_{EM}$  denotes the dimensional inertial position vector between the Earth and the Moon. The vector  $\vec{h}$  denotes the instantaneous angular momentum vector,  $\vec{h} = \vec{R}_{EM} \times \vec{V}_{EM}$ , where  $\times$  represents a cross product and  $\vec{V}_{EM}$  is the time derivative of  $\vec{R}_{EM}$ , tracking the dimensional inertial velocity vector between the Earth and the Moon. The symbol  $h$  is the magnitude of  $\vec{h}$ . These instantaneously constructed quantities  $l$  and  $\mathbf{C}$  corroborate to fix the Earth and the Moon within the pulsating-rotating frame as apparent from Fig. 2(c). The nd position vectors for the Earth and the Moon are fixed on the  $\hat{x}$ -axis as  $\vec{\rho}_E = -\mu\hat{x}$  and  $\vec{\rho}_M = (1 - \mu)\hat{x}$ , respectively, where  $\mu = \tilde{\mu}_M/(\tilde{\mu}_E + \tilde{\mu}_E)$  corresponds to the mass ratio of the Moon with respect to the Earth-Moon system. The pulsating-rotating frame serves as a common reference frame to represent all the dynamical models under the current investigation. Note that for the Earth-Moon CR3BP, the uniform-rotating frame and pulsating-rotating frame coincide as the Earth-Moon primary orbit remains circular.

Often, different independent variables are employed to describe dynamical models; ones that appear frequently in the current investigation are included in Table 2. First, the dimensional time is denoted as  $T$ , and the derivative with respect to this time is represented with the prime,  $(\cdot)'$ . Then, three nd time definitions are included in Table 2, illustrating the derivative symbols and the relationship to the dimensional time,  $T$ . Note that  $t_*$  flows uniformly with respect to the dimensional time, satisfying  $dt_*/dT = \sqrt{\tilde{\mu}_*/l_*^3}$ , where  $\tilde{\mu}_* = \tilde{\mu}_E + \tilde{\mu}_M$ . In contrast,  $t$  flows at a non-uniform rate, constructed with the pulsating instantaneous distance between Earth-Moon,  $l$ , resulting in  $dt/dT = \sqrt{\tilde{\mu}_*/l^3}$ . Thus, the labels “uniform nd time” and “pulsating nd time” are leveraged to describe these independent variables. The last type of independent variable, the Hill nd time, is defined such that  $d\tau/dT = 1/m\sqrt{\tilde{\mu}_S/l_{SB*}^3}$ . It is also assumed to satisfy  $d\tau/dt_* = 1/(1+m)$ . Thus, the Hill nd time scales the uniform nd time by  $(1+m)$ ; within the uniform nd time and Hill time,  $2\pi$  nd corresponds to the sidereal lunar month and synodic lunar month, respectively. To enable this scaling property,  $l_*$  is defined with the following ratio,

$$a_0 := \frac{l_*}{l_H} = \left( \frac{m}{1+m} \right)^{(2/3)} \approx 0.1775, \quad (5)$$

where  $l_H$  is defined from Eq. (1). However, with the mathematical consistency between the frames and independent variables aside, the choice of  $l_*$  does not influence the dynamics as described in nd units. For example, a value of

$$a_0 = m^{2/3}(1 - 2m/3 + 7m^2/18 - 4m^3/81) \approx 0.1774 \quad (6)$$

is leveraged in Scheeres (1998) for deriving the HR4BP based on Wintner (1947). While the current analysis adopts Eq. (5), the subsequent results are independent of such choice.

**Table 1:** Frames

	Hill frame	Uniform-rotating frame	Pulsating-rotating frame
Illustration	Fig. 2(a)	Fig. 2(b)	Fig. 2(c)
Position vector	$\vec{r}_{EM} = \xi\hat{i}_H + \eta\hat{j}_H + \zeta\hat{k}_H$	$\vec{\rho}_* = x_*\hat{x}_* + y_*\hat{y}_* + z_*\hat{z}_*$	$\vec{\rho} = x\hat{x} + y\hat{y} + z\hat{z}$
Unit vectors	$\hat{i}_H - \hat{j}_H - \hat{k}_H$	$\hat{x}_* - \hat{y}_* - \hat{z}_*$	$\hat{x} - \hat{y} - \hat{z}$
Relationship to $\vec{R}$	$\vec{R}_{EM} = l_H \mathbf{C}_H \vec{r}_{EM}$	$\vec{R} = \vec{B} + l_* \mathbf{C}_* \vec{\rho}_*$	$\vec{R} = \vec{B} + l \mathbf{C} \vec{\rho}$

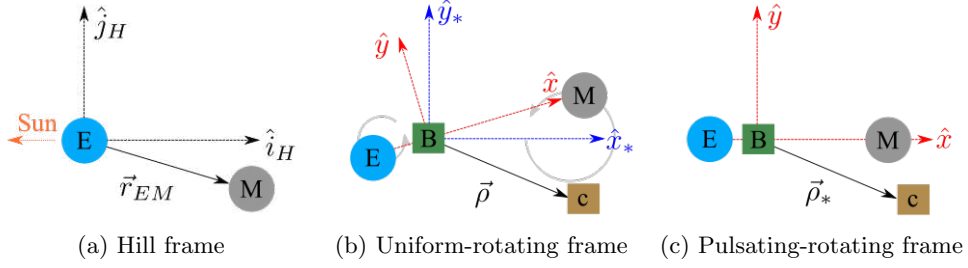


**Fig. 2:** Frame information

**Table 2:** Independent variables

Name	Dimensional time	Uniform nd time	Pulsating nd time	Hill nd time
Symbol	$T$	$t_*$	$t$	$\tau$
Derivative	$(\cdot)'$ [prime]	$(\cdot)^*$ [asterisk]	$(\cdot)^{\cdot}$ [dot]	$(\cdot)^{\circ}$ [circle]
Relationship to $T$	$\frac{dT}{dT} = 1$	$\frac{dt_*}{dT} = \sqrt{\frac{\mu_*}{l_*^3}}$	$\frac{dt}{dT} = \sqrt{\frac{\mu_*}{l_*^3}}$	$\frac{d\tau}{dT} = \frac{1}{m} \sqrt{\frac{\mu_S}{l_{SB*}^3}}$

## 2.2 Pulsating-Rotating Frame: Coefficient Representation

Gómez et al. (2002) provide a framework where the CR3BP and HFEM are represented within the pulsating-rotating frame (Fig. 2(c)). Such a formulation is initially reviewed. Originating from

$$\vec{R} = \vec{B} + l\vec{C}\vec{\rho}, \quad (7)$$

in Table 1, it is possible to derive the nd equations of motion for the spacecraft under a general dynamical model within the pulsating-rotating frame, resulting in,

$$\ddot{\vec{\rho}} = \begin{bmatrix} b_1 \\ b_2 \\ b_3 \end{bmatrix} + \begin{bmatrix} b_4 & b_5 & 0 \\ -b_5 & b_4 & b_6 \\ 0 & -b_6 & b_4 \end{bmatrix} \dot{\vec{\rho}} + \begin{bmatrix} b_7 & b_9 & b_8 \\ -b_9 & b_{10} & b_{11} \\ b_8 & -b_{11} & b_{12} \end{bmatrix} \vec{\rho} + b_{13} \nabla \Omega, \quad (8)$$

where the coefficients  $(b_i, i = 1, \dots, 13)$  are expressed as,

$$\begin{aligned} b_1 &= -\frac{\vec{B}'' \cdot \hat{x}}{(t')^2 l}, & b_2 &= -\frac{\vec{B}'' \cdot \hat{y}}{(t')^2 l}, & b_3 &= -\frac{\vec{B}'' \cdot \hat{z}}{(t')^2 l}, & b_4 &= -\frac{2l'}{t'l} - \frac{t''}{t'^2} \\ b_5 &= \frac{2h}{t'l}, & b_6 &= \frac{2l}{t'h} \vec{A}_{EM} \cdot \hat{z}, & b_7 &= -\frac{l''}{(t')^2 l} + \frac{h^2}{(t')^2 l^4} \\ b_8 &= -\frac{1}{(t')^2 l} \vec{A}_{EM} \cdot \hat{z}, & b_9 &= \frac{h'}{(t')^2 l^2}, \end{aligned}$$

$$\begin{aligned}
b_{10} &= -\frac{l''}{(t')^2 l} + \frac{h^2}{(t')^2 l^4} + \frac{l^2}{(t')^2 h^2} (\vec{A}_{EM} \cdot \hat{z})^2 \\
b_{11} &= \frac{3hl' - 2lh'}{(t')^2 h^2} \vec{A}_{EM} \cdot \hat{z} + \frac{1}{(t')^2 h} \vec{J}_{EM} \cdot \hat{z} \\
b_{12} &= -\frac{l''}{(t')^2 l} + \frac{l^2}{(t')^2 h^2} (\vec{A}_{EM} \cdot \hat{z})^2, \quad b_{13} = \frac{\tilde{\mu}_E + \tilde{\mu}_M}{l^3 (t')^2},
\end{aligned} \tag{9}$$

where  $\vec{A}_{EM}$  and  $\vec{J}_{EM}$  denote the relative dimensional acceleration and jerk vector between the Earth and the Moon, respectively, and  $\nabla\Omega$  is the gradient of the potential function  $\Omega$  defined as,

$$\Omega(\mu, \vec{\rho}, \tilde{\mu}_S, \vec{\rho}_S) = \frac{1-\mu}{\rho_{Ec}} + \frac{\mu}{\rho_{Mc}} + \frac{\mu_S}{\rho_{Sc}}, \quad \mu_S = \frac{\tilde{\mu}_S}{\tilde{\mu}_M + \tilde{\mu}_E}. \tag{10}$$

The subscript  $c$  denotes the spacecraft. Thus, the vectors  $\rho_{Ec}, \rho_{Mc}, \rho_{Sc}$  denote the distances from the spacecraft to the Earth, Moon, and Sun, respectively. Note that only the point-mass gravity from three celestial bodies, i.e., the Sun, Earth and Moon, is considered as influencing the motion of the spacecraft in the current investigation. However, a more general formulation is derived in Gómez et al. (2002); Dei Tos (2014); Park and Howell (2024b), where additional bodies may be added to  $\Omega$ . Further details for the derivation in Eq. (9) are available in Dei Tos (2014). Gómez et al. (2002) note there exists some arbitrariness in defining a suitable function for  $t' = \frac{dt}{dT}$  and  $t'' = \frac{d^2 t}{dT^2}$  that appear in the coefficients. Gómez et al. (2002) leverage the uniform time, i.e.,  $t_*$  from Table 2, to develop the equations of motion and the coefficient functions, resulting in expressions for  $\vec{\rho} = \frac{d^2 \vec{\rho}}{dt_*^2}$ . In such a formulation, they demonstrate that the Sun-Earth-Moon point-mass HFEM is associated with five distinct frequencies, where the coefficients  $b_{1-13}$  are approximated as quasi-periodic functions. These frequencies include  $\nu_{1,2,3}$ , associated with the anomalistic, synodic, and draconic lunar months, respectively. The physical interpretations of the frequencies are:  $\nu_1$  measures the average timing between lunar perigees that is the most dominant frequency for the Earth-Moon distance variation,  $\nu_2$  tracks the in-plane solar position within the pulsating-rotating frame, and  $\nu_3$  is linked to the out-of-plane solar position within the frame. Indeed, the common representation of the dynamical models facilitates recognition of the gap between the CR3BP and HFEM identified as force components originating from multiple frequencies. This formulation serves as a key step for constructing a suitable hierarchy in the Earth-Moon multi-body dynamical regime. The pulsating-rotating frame formulation is extendable to any intermediate models between the CR3BP and HFEM. Such efforts first appear in Dei Tos and Topputo (2017), where several intermediate models including the ER3BP are cast within the pulsating-rotating frame.

More recently, Park and Howell (2024b) introduce the concept of the pulsating time as defined in Table 2. Their adjustment reveals that by employing a non-uniform flow rate between the time and dimensional time that satisfies  $t' = \sqrt{(\tilde{\mu}_E + \tilde{\mu}_M)/l^3}$ , the velocity components between different models are suitably scaled and results

in  $b_{13} = 1$  for all dynamical models; it is then possible to isolate the CR3BP-originating accelerations and additional perturbations, facilitating the comparison between dynamical models that leverage different frames as well as independent variables. Based on this updated formulation, [Park and Howell \(2024b\)](#) compare the relative magnitude for perturbing accelerations that originate from  $\nu_{1,2}$ , the first two frequencies that characterize the time-dependent perturbations within the HFEM. Then, potential capabilities and limitations of two representative intermediate models, i.e., ER3BP and BCR4BP that approximately model  $\nu_1$ - and  $\nu_2$ -related perturbations, respectively, are examined by cataloging these models within the pulsating-rotating frame with respect to the pulsating time. This process results in Eq. (9) in the form of  $\ddot{\vec{\rho}} = \frac{d^2 \vec{\rho}}{dt^2}$ , rather than  $\ddot{\vec{\rho}}^{**}$  that is originally employed by [Gómez et al. \(2002\)](#).

### 3 Periodically Perturbed Models: Coherent Four-Body Problems

Extending the previous research efforts in utilizing the pulsating-rotating frame to analyze various dynamical models, the capabilities of two additional four-body dynamical models are investigated: the QBCP and HR4BP. These four-body models include a *coherent* representation for the solar gravity as compared to the BCR4BP. Questions exist in characterizing the coherent solar gravity in terms of the coefficients,  $b_{1-13}$  from Eq. (9), in comparison with the HFEM as well as the BCR4BP. Also, the similarities and differences between the QBCP and HR4BP in a global sense across cislunar space remains elusive. To answer these questions, the general analytical properties for coherent solar gravity modeling within the pulsating-rotating equations of motion are first discussed [Goal (G1) from Section 1.1]. Then, leveraging the derivations from previous authors ([Andreu, 1998](#); [Scheeres, 1998](#)), the equations of motion for the QBCP and HR4BP are re-derived in the form of  $\ddot{\vec{\rho}}$  from Eq. (9) by transforming the frames and/or independent variables [Goal (G2) from Section 1.1].

#### 3.1 Coherent Solar Gravity Modeling

The coherent representation of the solar gravity within the Earth-Moon system is properly defined. In general, the coherency refers to a characteristic of the dynamical model where the motion of the celestial bodies is solely explained by mutual dynamical forces. While this criterion seems binary, in reality, a spectrum of coherency exists where some models are considered “more” coherent than others. For example, consider the ephemerides for the solar system generated via mutual point-mass gravitational forces as well as tidal forces between the Earth-Moon and the solar radiation pressure, e.g., DE 440/441 from Jet Propulsion Laboratory ([Park et al., 2021](#)). Including only the Earth-Moon-Sun point-mass gravity into the model technically is not a coherent representation of the systems as the ephemerides do not originate solely from the Earth-Moon-Sun point-mass gravity model. However, such model may be considered more coherent than the Earth-Moon point-mass gravity model that is incapable of producing the non-Keplerian motion for the realistic Earth-Moon system under the influence of the Sun.

In understanding the capabilities of different four-body models that include Earth-Moon-Sun as the celestial bodies influencing the spacecraft, the coherent solar gravity modeling plays a crucial role. In general, the QBCP and HR4BP are considered to be “more coherent”, supplying a time-varying Earth-Moon distance in the presence of the solar gravity as opposed to the BCR4BP where the Earth-Moon motion remains circular. In the current analysis, the coherent solar gravity modeling is straightforwardly evaluated within the pulsating-rotating frame formulation, leveraging insights from [Park and Howell \(2024b\)](#). They classify the following terms as generally associated with the solar gravity,

$$\ddot{\vec{\rho}}_{Solar} := \underbrace{\begin{bmatrix} b_1 \\ b_2 \\ b_3 \end{bmatrix}}_{(i)} + \begin{bmatrix} 0 & 0 & 0 \\ 0 & 0 & b_6 \\ 0 & -b_6 & 0 \end{bmatrix} \dot{\vec{\rho}} + \underbrace{\begin{bmatrix} b_7 - 1 & b_9 & b_8 \\ -b_9 & b_{10} - 1 & b_{11} \\ b_8 & -b_{11} & b_{12} - b_{12a} \end{bmatrix}}_{(ii)} \vec{\rho} + \underbrace{b_{13} \nabla \left( \frac{\mu_S}{\rho_{Sc}} \right)}_{(iii)} \quad (11)$$

where  $b_{12a} = -\frac{l''}{(t')^2 l}$ . Note that while the solar gravity influences all the coefficients  $b_{1-13}$  simultaneously, three notable sources are identified as: (i) indirect gravity on the Earth-Moon barycenter,  $b_{1-3}$ , (ii) frame rotation,  $b_{7-10}$ , (iii) direct gravity on the spacecraft,  $b_{13} \nabla \Omega$ . Assuming that the Earth-Moon-Sun motion is coherently represented by mutual point-mass gravity forces, [Park and Howell \(2024b\)](#) demonstrate that (i)-(iii) mutually cancel each other, resulting in,

$$\ddot{\vec{\rho}}_{Solar} = \ddot{\vec{\rho}}_{Solar,G} + \begin{bmatrix} 0 & 0 & 0 \\ 0 & 0 & b_6 \\ 0 & -b_6 & 0 \end{bmatrix} \dot{\vec{\rho}} + \begin{bmatrix} 0 & 0 & 0 \\ 0 & b_{12} - b_{12a} & b_{11} \\ 0 & -b_{11} & b_{12} - b_{12a} \end{bmatrix} \vec{\rho}. \quad (12)$$

Then,  $\ddot{\vec{\rho}}_{Solar,G}$  denotes the “pseudo-gravity” term that analytically simplifies into the following form,

$$\begin{aligned} \ddot{\vec{\rho}}_{Solar,G} \cdot \hat{x} &= -\frac{1}{\rho_{Sc}^3}(x - x_S) - \frac{1}{\rho_{SE}^3}(x - 1 + \mu)(-\mu - x_S) + \frac{1}{\rho_{SM}^3}(x + \mu)(1 - \mu - x_S) \\ &\quad + \frac{1}{\rho_{SE}^3}y(-y_S) - \frac{1}{\rho_{SM}^3}y(-y_S) - \frac{1}{\rho_{SE}^3}z(-z_S) + \frac{1}{\rho_{SM}^3}z(-z_S), \\ \ddot{\vec{\rho}}_{Solar,G} \cdot \hat{y} &= -\frac{1}{\rho_{Sc}^3}(y - y_S) - \frac{1}{\rho_{SE}^3}(x - 1 + \mu)(-y_S) + \frac{1}{\rho_{SM}^3}(x + \mu)(-y_S) \\ &\quad - \frac{1}{\rho_{SE}^3}y(-\mu - x_S) + \frac{1}{\rho_{SM}^3}y(1 - \mu - x_S), \\ \ddot{\vec{\rho}}_{Solar,G} \cdot \hat{z} &= -\frac{1}{\rho_{Sc}^3}(z - z_S) - \frac{1}{\rho_{SE}^3}(x - 1 + \mu)(-z_S) + \frac{1}{\rho_{SM}^3}(x + \mu)(-z_S) \end{aligned} \quad (13)$$

where  $\vec{\rho}_S = x_S \hat{x} + y_S \hat{y} + z_S \hat{z}$  denotes the nd solar position vector within the pulsating-rotating frame. The expressions do not involve any coefficients from Eq. (9); rather, they are represented in a straightforward manner involving only the position vectors for the Sun and spacecraft. Thus, the mutual cancellation of the terms (i)-(iii) is equivalent

to the coherent solar gravity modeling as viewed within the pulsating-rotating frame, resulting in Eq. (13). Further intuition is generated via a linearization process from Park and Howell (2024b), noting that  $\rho_{SB} \approx 400 \gg \rho_{EM} = 1$ , resulting in,

$$\frac{1}{\rho_{Sj}^3} \approx \frac{1}{\rho_S^3} + \frac{3}{\rho_S^5}(\vec{\rho}_S \cdot \vec{\rho}_j), \quad j = E, M, c. \quad (14)$$

Applying this linearization to Eq. (13),

$$\begin{aligned} \ddot{\vec{\rho}}_{Solar,G} \cdot \hat{x} &\approx \frac{3\mu_S}{\rho_S^5} (2x_S y_S y) + O(\rho_S^{-4}) \\ \ddot{\vec{\rho}}_{Solar,G} \cdot \hat{y} &\approx \frac{3\mu_S}{\rho_S^5} ((y_S^2 - x_S^2)y + y_S z_S z) + O(\rho_S^{-4}) \\ \ddot{\vec{\rho}}_{Solar,G} \cdot \hat{z} &\approx \frac{3\mu_S}{\rho_S^5} (y_S z_S y + (\rho_S^2 + z_S^2)z) + O(\rho_S^{-4}), \end{aligned} \quad (15)$$

where  $O(\rho_S^{-4})$  is the higher-order influence from the powers of  $\rho_S$  that is generally associated with smaller magnitudes. In addition, if the spacecraft remains in-plane within the pulsating-rotating frame,  $z = 0$ , and if the out-of-plane solar position component is negligible,  $z_S \approx 0$ , the expression further simplifies to,

$$\ddot{\vec{\rho}}_{Solar,G} \approx \frac{3\mu_S}{\rho_S^3} (\cos 2\theta_S \hat{x} - \sin 2\theta_S \hat{y}), \quad (16)$$

where  $0 \leq \theta_S \leq 2\pi$  measures the in-plane solar position angle, i.e.,  $\cos(\theta_S) = x_S/\rho_S$ . The significance of this expression is that the magnitude originating from the solar gravity appears to be almost independent of the  $\hat{x}$ -position within the pulsating-rotating frame. For the two coherent four-body models, i.e., QBCP and HR4BP, the general characteristics of coherent solar gravity modeling are represented by Eqs. (13), (15), and (16), a property that is discussed in subsequent sections.

### 3.2 Quasi Bi-Circular Problem (QBCP)

The QBCP, introduced by Andreu (1998), represents a fully coherent four-body modeling; the equations of motion for the spacecraft are described within the Earth-Moon-Sun system under mutual point-mass gravitational influence. Hence, the motion of the Earth-Moon-Sun system is a particular solution for the three-body problem comprised of the three celestial bodies. To supply a periodically forced model within the pulsating-rotating frame, the motion of the celestial bodies is confined to a common plane, and, the Earth-Moon and Sun- $B$  motion each follows a nearly circular trajectory. The relative position vectors between Earth-Moon and Sun- $B$  are represented as Fourier series that involve a single frequency,  $\nu_2$ , associated with the synodic lunar month. In Andreu (1998), a semi-analytical procedure is illustrated to sequentially compute coefficients for the Fourier series while satisfying the differential equations provided by the Earth-Moon-Sun three-body problem. Then, utilizing the relative

position vectors for the Earth-Moon and Sun- $B$ , the equations of motion for the spacecraft are described within the pulsating-rotating frame. The expression reads (Andreu, 1998; Gao et al., 2022),

$$\begin{aligned}
\ddot{x} &= \frac{\dot{\alpha}_1}{\alpha_1} \dot{x} + \left( -\frac{\dot{\alpha}_1 \alpha_2}{\alpha_1} + \ddot{\alpha}_2 + \alpha_2^2 + \alpha_3^2 \right) x + 2\alpha_3 \dot{y} + \left( -\frac{\dot{\alpha}_1 \alpha_3}{\alpha_1} + \dot{\alpha}_3 \right) y \\
&\quad - \alpha_1 \alpha_4 - \alpha_1 \alpha_6 \left( \frac{1-\mu}{\rho_{Ec}^3} (x-\mu) + \frac{\mu}{\rho_{Mc}^3} (x-\mu+1) + \frac{\mu_S}{\rho_{Sc}^3} (x+\alpha_7) \right) \\
\ddot{y} &= \frac{\dot{\alpha}_1}{\alpha_1} \dot{y} + \left( -\frac{\dot{\alpha}_1 \alpha_2}{\alpha_1} + \ddot{\alpha}_2 + \alpha_2^2 + \alpha_3^2 \right) y - 2\alpha_3 \dot{x} + \left( \frac{\dot{\alpha}_1 \alpha_3}{\alpha_1} - \dot{\alpha}_3 \right) x \\
&\quad - \alpha_1 \alpha_5 - \alpha_1 \alpha_6 \left( \frac{1-\mu}{\rho_{Ec}^3} y + \frac{\mu}{\rho_{Mc}^3} y + \frac{\mu_S}{\rho_{Sc}^3} (y+\alpha_8) \right) \\
\ddot{z} &= \frac{\dot{\alpha}_1}{\alpha_1} \dot{z} + \left( -\frac{\dot{\alpha}_1 \alpha_2}{\alpha_1} + \ddot{\alpha}_2 + \alpha_2^2 \right) z - \alpha_1 \alpha_6 \left( \frac{1-\mu}{\rho_{Ec}^3} z + \frac{\mu}{\rho_{Mc}^3} z + \frac{\mu_S}{\rho_{Sc}^3} z \right),
\end{aligned} \tag{17}$$

where the independent variable is selected as the uniform time,  $t_*$ , in Andreu (1998). The  $\alpha_{1-8}$  quantities correspond to  $\nu_2$ -periodic functions that derive from the relative Earth-Moon and Sun- $B$  position vectors. These functions are represented as sine and cosine series, where the coefficients for each order are provided in Andreu (1998), and recalled in Tables A1-A3 from Appendix A. While Andreu (1998)'s original formulation assumes the Earth and Moon to be located at  $(\mu, 0, 0)$  and  $(-1+\mu, 0, 0)$  within the pulsating-rotating frame, the current work adopts the locations as  $(-\mu, 0, 0)$  and  $(1-\mu, 0, 0)$ , respectively, to be consistent with other dynamical models. Thus, Eq. (17) as well as some Fourier coefficients within Tables A1-A3 are adjusted from Andreu (1998) to mirror this directional change.

In the current analysis, the QBCP dynamics are re-cast with respect to the pulsating time. Such a process involves the independent variable change from  $t_*$  to  $t$  and, retrieving  $b_{1-13}$ ,  $1 \leq i \leq 13$  in terms of Andreu (1998)'s  $\nu_2$ -periodic functions,  $\alpha_{1-8}$ . Noting the physical interpretations for  $\alpha_{1-8}$  (Eq. (A1) from Appendix A),  $b_{1-13}$  are expressed as,

$$\begin{aligned}
b_1 &= \frac{\alpha_1 \alpha_4}{\alpha_6^3}, \quad b_2 = \frac{\alpha_1 \alpha_5}{\alpha_6^3}, \quad b_4 = \frac{\dot{\alpha}_1}{4\alpha_1 \alpha_6^{3/2}} = \frac{\alpha_2}{2\alpha_6^{3/2}}, \quad b_5 = \frac{2\alpha_3}{\alpha_6^{3/2}} \\
b_7 &= b_{10} = -\frac{\dot{\alpha}_1 \alpha_2}{\alpha_1 \alpha_6^3} + \frac{\dot{\alpha}_2}{\alpha_6^3} + \frac{\alpha_2^2}{\alpha_6^3} + \frac{\alpha_3^2}{\alpha_6^3}, \quad b_9 = -\frac{\dot{\alpha}_1 \alpha_3}{\alpha_1 \alpha_6^3} + \frac{\dot{\alpha}_3}{\alpha_6^3} \\
b_{12} &= -\frac{\dot{\alpha}_1 \alpha_2}{\alpha_1 \alpha_6^3} + \frac{\dot{\alpha}_2}{\alpha_6^3} + \frac{\alpha_2^2}{\alpha_6^3}, \quad b_{13} = \frac{\alpha_1 \alpha_6}{\alpha_6^3} = 1, \quad b_3 = b_6 = b_8 = b_{11} = 0,
\end{aligned} \tag{18}$$

concluding the derivation for the QBCP within the pulsating-rotating frame with respect to the pulsating time. Note that the zero coefficients occur as the QBCP assumes a coplanar motion for the Sun-Earth-Moon system and, thus, many out-of-plane directional components are zeros, e.g.,  $\vec{A}_{EM} \cdot \hat{z}$ .



### 3.3 Hill Restricted Four-Body Problem (HR4BP)

The HR4BP is another example of a coherent four-body model as described initially by [Mohn and Kevorkin \(1967\)](#) and later elaborated by [Scheeres \(1998\)](#). The model introduces the Hill approximation, i.e.,  $\tilde{\mu}_S \gg \tilde{\mu}_E + \tilde{\mu}_M$  and  $\rho_S \gg 1$ , to the general Earth-Moon-Sun three-body problem, and is distinguished from the QBCP. The relative motion for the Earth-Moon system is described within the HR3BP formulation under this approximation. Then, [Scheeres \(1998\)](#) introduces a generic framework where any particular solution from the HR3BP may be leveraged to represent a four-body model employing the Hill approximation within the uniform-rotating frame (Fig. 2(b)). To formulate the problem, [Scheeres \(1998\)](#) selects one particular periodic orbit within the HR3BP that is known as the “lunar variational orbit,” expressed via Fourier series approximation to the required order ([Wintner, 1947](#); [Scheeres, 1998](#); [Olikara and Scheeres, 2017](#)) leveraging the  $\nu_2$  frequency. The four-body model results in a periodically forced formulation within the uniform-rotating frame, deriving the HR4BP dynamics.

While the current analysis leverages the derivations and insights from the original work from [Scheeres \(1998\)](#) for the HR4BP, it adopts the pulsating-rotating frame to facilitate the assessment of the HR4BP within the context of the hierarchy of different dynamical models. For the derivation of HR4BP within the pulsating-rotating frame, first consider the HR3BP as represented within the Hill frame (Fig. 2(a)) with respect to the Hill nd time,  $\tau$ ,

$$\begin{aligned}\ddot{\xi} &= 2m\dot{\eta} + 3m^2\xi - \frac{m^2}{r_{EM}^3}\xi \\ \ddot{\eta} &= -2m\dot{\xi} - \frac{m^2}{r_{EM}^3}\eta \\ \ddot{\zeta} &= -m^2\zeta - \frac{m^2}{r_{EM}^3}\zeta,\end{aligned}\tag{19}$$

where  $\vec{r}_{EM} = \xi\hat{i}_H + \eta\hat{j}_H + \zeta\hat{k}_H$  denotes the nd lunar position from the Earth within the frame. Typically in the literature ([Scheeres, 1998](#)), the HR3BP is described with respect to an independent variable defined as  $m\tau$ . In such a case, the parameter  $m$  does not appear within the HR3BP equations of motion. To represent the HR4BP within the pulsating-rotating frame, the unit vectors for the pulsating-rotating frame, i.e.,  $\hat{x} - \hat{y} - \hat{z}$ , are represented with respect to the quantities within the Hill frame, i.e.,  $\xi, \eta, \zeta$ . For computing the unit vectors, consider the following rotation between the Hill frame nd Earth-Moon vector,  $\vec{r}_{EM}$ , and the uniform-rotating frame nd Earth-Moon vector,  $\vec{\rho}_{EM,*}$ , utilizing the expressions from Table 1,

$$\vec{\rho}_{EM,*} = \frac{l_H \mathbf{C}_H^* \vec{r}_{EM}}{l_*} = \frac{\mathbf{C}_H^* \vec{r}_{EM}}{a_0} = x_{EM,*} \hat{x}_* + y_{EM,*} \hat{y}_* + z_{EM,*} \hat{z}_*,\tag{20}$$

where  $\mathbf{C}_H^*$  is the direction cosine matrix from the Hill frame to the uniform-rotating frame computed from Eqs. (2)-(3) and  $a_0$  is a scaling factor from Eq. (5),

$$\mathbf{C}_H^* = \begin{bmatrix} \cos \tau & \sin \tau & 0 \\ -\sin \tau & \cos \tau & 0 \\ 0 & 0 & 1 \end{bmatrix}. \quad (21)$$

Then,

$$x_{EM*} = \frac{\xi \cos \tau + \eta \sin \tau}{a_0}, \quad y_{EM*} = \frac{-\xi \sin \tau + \eta \cos \tau}{a_0}, \quad z_{EM*} = \frac{\zeta}{a_0}. \quad (22)$$

The derivatives of  $x_{EM*}, y_{EM*}, z_{EM*}$  with respect to the Hill time,  $\tau$ , are,

$$\begin{aligned} \dot{x}_{EM*} &= \frac{\dot{\xi} \cos \tau - \xi \sin \tau + \dot{\eta} \sin \tau + \eta \cos \tau}{a_0} \\ \ddot{x}_{EM*} &= \frac{\ddot{\xi} \cos \tau - 2\dot{\xi} \sin \tau - \xi \cos \tau + \ddot{\eta} \sin \tau + 2\dot{\eta} \cos \tau - \eta \sin \tau}{a_0} \\ \overset{\circ}{\ddot{x}}_{EM*} &= \frac{1}{a_0} \left( \overset{\circ}{\ddot{\xi}} \cos \tau - 3\overset{\circ}{\dot{\xi}} \sin \tau - 3\overset{\circ}{\dot{\xi}} \cos \tau + \xi \sin \tau \dots \right. \\ &\quad \left. + \overset{\circ}{\ddot{\eta}} \sin \tau + 3\overset{\circ}{\dot{\eta}} \cos \tau - 3\overset{\circ}{\dot{\eta}} \sin \tau - \eta \cos \tau \right) \\ \dot{y}_{EM*} &= \frac{-\dot{\xi} \sin \tau - \xi \cos \tau + \dot{\eta} \cos \tau - \eta \sin \tau}{a_0} \\ \ddot{y}_{EM*} &= \frac{-\ddot{\xi} \sin \tau - 2\dot{\xi} \cos \tau + \xi \sin \tau + \ddot{\eta} \cos \tau - 2\dot{\eta} \sin \tau - \eta \cos \tau}{a_0} \\ \overset{\circ}{\ddot{y}}_{EM*} &= \frac{1}{a_0} \left( -\overset{\circ}{\ddot{\xi}} \sin \tau - 3\overset{\circ}{\dot{\xi}} \cos \tau + 3\overset{\circ}{\dot{\xi}} \sin \tau + \xi \cos \tau \dots \right. \\ &\quad \left. + \overset{\circ}{\ddot{\eta}} \cos \tau - 3\overset{\circ}{\dot{\eta}} \sin \tau - 3\overset{\circ}{\dot{\eta}} \cos \tau + \eta \sin \tau \right) \\ \dot{z}_{EM*} &= \frac{\dot{\zeta}}{a_0}, \quad \ddot{z}_{EM*} = \frac{\ddot{\zeta}}{a_0}, \quad \overset{\circ}{\ddot{z}}_{EM*} = \frac{\overset{\circ}{\ddot{\zeta}}}{a_0}. \end{aligned} \quad (23)$$

Note that the quantities  $\overset{\circ}{\ddot{\xi}}, \overset{\circ}{\ddot{\eta}}, \overset{\circ}{\ddot{\zeta}}$  are evaluated along a selected HR3BP trajectory that represents the Earth-Moon relative motion, e.g., the lunar variational orbit. Then, the derivative of Eq. (20) results in,

$$\begin{aligned} \overset{\circ}{\vec{\rho}}_{EM*} &= (\dot{x}_{EM*} \hat{x}_* + \dot{y}_{EM*} \hat{y}_* + \dot{z}_{EM*} \hat{z}_*) + (1+m) \hat{z}_* \times \vec{\rho}_{EM*} \\ &= \left( \dot{x}_{EM*} - (1+m)y_{EM*} \right) \hat{x}_* + \left( \dot{y}_{EM*} + (1+m)x_{EM*} \right) \hat{y}_* + \dot{z}_{EM*} \hat{z}_*, \end{aligned} \quad (24)$$

where it is noted that  $\dot{t}_* = dt_*/d\tau = 1+m$  for evaluating the derivative of  $\mathbf{C}_*$  from Eq. (3), with respect to  $\tau$ . Then, a similar process is repeated to supply the acceleration

and jerk expressions as observed within the inertial frame as,

$$\begin{aligned}
\overset{\circ\circ}{\vec{\rho}}_{EM*} &= \left( \overset{\circ\circ}{x}_{EM*} - 2(1+m)\overset{\circ}{y}_{EM*} - (1+m)^2 x_{EM*} \right) \hat{x}_* \\
&\quad + \left( \overset{\circ\circ}{y}_{EM*} + 2(1+m)\overset{\circ}{x}_{EM*} - (1+m)^2 y_{EM*} \right) \hat{y}_* + \overset{\circ\circ}{z}_{EM*} \hat{z}_* \\
\overset{\circ\circ\circ}{\vec{\rho}}_{EM*} &= \left( \overset{\circ\circ\circ}{x}_{EM*} - 3(1+m)\overset{\circ\circ}{y}_{EM*} - 3(1+m)^2 \overset{\circ}{x}_{EM*} + (1+m)^3 y_{EM*} \right) \hat{x}_* \\
&\quad + \left( \overset{\circ\circ\circ}{y}_{EM*} + 3(1+m)\overset{\circ\circ}{x}_{EM*} - 3(1+m)^2 \overset{\circ}{y}_{EM*} - (1+m)^3 x_{EM*} \right) \hat{y}_* \\
&\quad + \overset{\circ\circ\circ}{z}_{EM*} \hat{z}_*.
\end{aligned} \tag{25}$$

Utilizing these expressions, the unit vectors within the pulsating-rotating frame (Fig. 2(c)) are *instantaneously* constructed as follows,

$$\begin{aligned}
\hat{x} &= \frac{x_{EM*} \hat{x}_* + y_{EM*} \hat{y}_* + z_{EM*} \hat{z}_*}{|\vec{\rho}_{EM*}|} \\
\hat{z} &= \frac{\vec{\rho}_{EM*} \times \overset{\circ}{\vec{\rho}}_{EM*}}{|\vec{\rho}_{EM*} \times \overset{\circ}{\vec{\rho}}_{EM*}|} \\
\hat{y} &= \hat{z} \times \hat{x},
\end{aligned} \tag{26}$$

where  $|\vec{\cdot}|$  denotes the l2-norm operator for a vector. The instantaneous non-dimensional Earth-Moon distance and its derivatives are then determined as,

$$\begin{aligned}
\rho_{EM*} &= |\vec{\rho}_{EM*}| = \sqrt{x_{EM*}^2 + y_{EM*}^2 + z_{EM*}^2} \\
\dot{\rho}_{EM*} &= \frac{x_{EM*} \dot{x}_{EM*} + y_{EM*} \dot{y}_{EM*} + z_{EM*} \dot{z}_{EM*}}{\rho_{EM*}} \\
\ddot{\rho}_{EM*} &= \frac{\dot{x}_{EM*} x_{EM*} + \dot{y}_{EM*} y_{EM*} + \dot{z}_{EM*} z_{EM*} + \dot{x}_{EM*}^2 + \dot{y}_{EM*}^2 + \dot{z}_{EM*}^2 - \dot{\rho}_{EM*}^2}{\rho_{EM*}}.
\end{aligned} \tag{27}$$

The dimensional Earth-Moon distance and its derivatives with respect to the dimensional time are computed with the expressions in Tables 1-2 as,

$$l = \rho_{EM*} l_*, \quad l' = \dot{\rho}_{EM*} \tau' l_*, \quad l'' = \ddot{\rho}_{EM*} (\tau')^2 l_*, \tag{28}$$

where it is noted that  $\tau' = d\tau/dT = 1/m\sqrt{\tilde{\mu}_S/l_{SB*}^3}$  (Table 2) and  $\frac{d^2\tau}{dT^2} = 0$ . Then, the dimensional position vector and its derivatives between the Earth and the Moon evolve as,

$$\vec{R}_{EM} = l_* \vec{\rho}_{EM*}, \quad \vec{V}_{EM} = l_* \tau' \overset{\circ}{\vec{\rho}}_{EM*}$$

$$\vec{A}_{EM} = l_*(\tau')^2 \vec{\rho}_{EM*}^{\circ\circ}, \quad \vec{J}_{EM} = l_*(\tau')^3 \vec{\rho}_{EM*}^{\circ\circ\circ}. \quad (29)$$

Additionally, the dimensional angular momentum magnitude as defined for the Earth-Moon system and its derivatives are determined as,

$$h = |\vec{R}_{EM} \times \vec{V}_{EM}|, \quad h' = (\vec{R}_{EM} \times \vec{A}_{EM}) \cdot \hat{z}. \quad (30)$$

With these dimensional quantities, the expressions  $b_{1-13}$  from Eq. (9) are evaluated for the HR4BP. In addition, the ‘‘Hill approximation’’ is leveraged as (Scheeres, 1998),

$$\frac{\vec{\rho}_{Sj}}{\rho_{Sj}^3} \approx \frac{\gamma \vec{\rho}_S}{(\gamma \rho_S)^3} + \frac{\vec{\rho}_j}{(\gamma \rho_S)^3} + \frac{3\gamma \vec{\rho}_S}{(\gamma \rho_S)^5} (\gamma \vec{\rho}_S \cdot \vec{\rho}_j), \quad j = E, M, c, \quad (31)$$

drawing similarities from the linearization process as introduced in Eq. (14). The constant  $\gamma = 1 - (\tilde{\mu}_E + \tilde{\mu}_M)/\tilde{\mu}_S \approx 1$  technically distinguishes the Hill approximation from the linearization process. However, in Scheeres (1998),  $\gamma = 1$  is enforced during the process of selecting a suitable dimensionalization quantity across different frames. Thus, the Hill approximation that appears in Scheeres (1998) is equivalent to the linearization described in Eq. (14). The expressions for  $b_{1-3}$  involve the acceleration of the Earth-Moon barycenter,  $\vec{B}''$ , due to the solar gravity. Applying the Hill approximation, it is evaluated as  $\vec{B}'' \approx -\frac{\tilde{\mu}_S}{l_{SB*}^2} \hat{i}_H$ , leading to the following first three coefficients within the HR4BP,

$$b_1 = \frac{\tilde{\mu}_S}{l(t')^2 l_{SB*}^2} \hat{i}_H \cdot \hat{x}, \quad b_2 = \frac{\tilde{\mu}_S}{l(t')^2 l_{SB*}^2} \hat{i}_H \cdot \hat{y}, \quad b_3 = \frac{\tilde{\mu}_S}{l(t')^2 l_{SB*}^2} \hat{i}_H \cdot \hat{z}. \quad (32)$$

The simple expression for  $\vec{B}''$  results from the fact that the Sun- $B$  follows a circular path within an inertial frame, an assumption introduced in the original formulation for the HR4BP from Scheeres (1998), or,  $l_{SB*}$  is constant. Thus,  $\vec{B} = -l_{SB*} \hat{i}_H$  within the Hill frame. The rest of the coefficients,  $b_{4-13}$ , are constructed from evaluating the Eq. (9) with the quantities from Eqs. (28)-(30). Lastly, the solar gravity terms for the gradient of the potential function,  $\nabla \Omega$ , from Eq. (10), is evaluated with the Hill approximation as,

$$\begin{aligned} \nabla \left( \frac{\mu_S}{\rho_{Sc}} \right) &= -\frac{\mu_S \vec{\rho}_{Sc}}{\rho_{Sc}^3} \approx -\mu_S \left( \frac{\vec{\rho}_S}{\rho_S^3} + \frac{\vec{\rho}}{\rho_S^3} + \frac{3\vec{\rho}_S}{\rho_S^5} (\vec{\rho}_S \cdot \vec{\rho}) \right) \\ &= -\frac{\tilde{\mu}_S}{l(t')^2 l_{SB*}^2} \hat{i}_H - \frac{\tilde{\mu}_S}{(t')^2 l_{SB*}^3} \vec{\rho} - \frac{3\tilde{\mu}_S}{(t')^2 l_{SB*}^3} (\hat{i}_H \cdot \vec{\rho}) \hat{i}_H, \end{aligned} \quad (33)$$

where  $(t')^2 = \frac{\tilde{\mu}_E + \tilde{\mu}_M}{l^3}$  and  $\vec{\rho}_S = \frac{l_{SB*}}{l} \hat{i}_H$  are leveraged in the derivation. Therefore, combining Eqs. (10) and (33),

$$\nabla \Omega = \underbrace{-\frac{\tilde{\mu}_S}{l(t')^2 l_{SB*}^2} \hat{i}_H}_{H_1} + \underbrace{-\frac{\tilde{\mu}_S}{(t')^2 l_{SB*}^3} \vec{\rho} - \frac{3\tilde{\mu}_S}{(t')^2 l_{SB*}^3} (\hat{i}_H \cdot \vec{\rho}) \hat{i}_H}_{H_2} + \underbrace{\nabla \left( \frac{1-\mu}{\rho_{Ec}} + \frac{\mu}{\rho_{Mc}} \right)}_{\nabla \Omega_{CR3BP}}. \quad (34)$$

The  $\nabla\Omega$  components in the unit vectors for the pulsating rotating frame, e.g.,  $\nabla\Omega_x$ , are retrieved as,

$$\Omega_x = -\frac{\tilde{\mu}_S}{l(t')^2 l_{SB*}^2} \left( (\hat{i}_H \cdot \hat{x}) + \frac{l}{l_{SB*}} x - \frac{3l}{l_{SB*}} \left( x(\hat{i}_H \cdot \hat{x}) + y(\hat{i}_H \cdot \hat{y}) + z(\hat{i}_H \cdot \hat{z}) \right) (\hat{i}_H \cdot \hat{x}) \right) + \frac{(1-\mu)(x+\mu)}{d^3} - \frac{\mu(x-(1-\mu))}{r^3}. \quad (35)$$

Note that  $\hat{i}_H = \cos\tau\hat{x}_* - \sin\tau\hat{y}_*$  from Eq. (21) is used in combination with Eq. (26) to define the dot product between  $\hat{i}_H$  and  $\hat{x} - \hat{y} - \hat{z}$ , the unit vectors in the pulsating-rotating frame.

Additional insights are available for the HR4BP dynamics as cast within the pulsating-rotating frame with respect to the pulsating nd time. Firstly, observe that  $b_{13}$  is always unity under the pulsating nd time; then, the  $H_1$  term from Eq. (34) is identical to the  $b_{1-3}$  functions from Eq. (32) but opposite in signs. Thus, analytical cancellations exist between the indirect gravity and some terms for the direct gravity from the Sun, alluding to the coherent nature of the HR4BP dynamics even under the Hill approximation. Furthermore, since the linear approximation from Eq. (14) is equivalent to the Hill approximation, the simplified solar gravity expressions within any coherent solar gravity modeling as listed in Eq. (15) are expected to be representative of the HR4BP dynamics. Thus, three different representations for the HR4BP are available within the pulsating-rotating frame with respect to the pulsating nd time as,

$$\ddot{\vec{\rho}} = \begin{bmatrix} b_1 \\ b_2 \\ b_3 \end{bmatrix} + \begin{bmatrix} b_4 & b_5 & 0 \\ -b_5 & b_4 & b_6 \\ 0 & -b_6 & b_4 \end{bmatrix} \dot{\vec{\rho}} + \begin{bmatrix} b_7 & b_9 & b_8 \\ -b_9 & b_{10} & b_{11} \\ b_8 & -b_{11} & b_{12} \end{bmatrix} \vec{\rho} + b_{13} \nabla\Omega \quad (36)$$

$$= \begin{bmatrix} b_4 & b_5 & 0 \\ -b_5 & b_4 & b_6 \\ 0 & -b_6 & b_4 \end{bmatrix} \dot{\vec{\rho}} + \begin{bmatrix} b_7 & b_9 & b_8 \\ -b_9 & b_{10} & b_{11} \\ b_8 & -b_{11} & b_{12} \end{bmatrix} \vec{\rho} + H_2 + \nabla\Omega_{CR3BP} \quad (37)$$

$$= \ddot{\vec{\rho}}_{CR3BP} + \begin{bmatrix} b_4 & b_5 - 2 & 0 \\ -b_5 + 2 & b_4 & b_6 \\ 0 & -b_6 & b_4 \end{bmatrix} \dot{\vec{\rho}} + \frac{3\mu_S}{\rho_S^5} \begin{bmatrix} 0 & 2x_S y_S & 0 \\ 0 & y_S^2 - x_S^2 & y_S z_S \\ 0 & y_S z_S & \rho_S^2 + z_S^2 \end{bmatrix} \vec{\rho} + \begin{bmatrix} 0 & 0 & 0 \\ 0 & b_{12} - b_{12a} & b_{11} \\ 0 & -b_{11} & b_{12} \end{bmatrix} \vec{\rho}. \quad (38)$$

The first equation, Eq. (36), corresponds to the full HR4BP representation without any cancellation between the terms. Then, Eq. (37) illustrates a partially cancelled formulation between  $b_{1-3}$  and  $H_1$  from Eq. (34). Lastly, Eq. (38) denotes a fully simplified HR4BP dynamics where a significantly fewer number of coefficients,  $b_i$ , are required to represent the dynamics. Here,  $\ddot{\vec{\rho}}_{CR3BP}$  is evaluated as  $\ddot{\vec{\rho}}_{CR3BP} = -2\hat{z} \times \dot{\vec{\rho}} + x\hat{x} + y\hat{y} + \nabla\Omega_{CR3BP}$ , the CR3BP portion of the dynamics given a particular spacecraft state within the pulsating-rotating frame. It is emphasized that these three equations of motion, Eqs. (36)-(38), are different representations of the same dynamics,

yielding multiple analytical insights. All three expressions are in mutual agreement under numerical tests to the machine precision.

In practice, it is beneficial to consider the pulsating-rotating frame equations of motion but described with respect to the Hill time,  $\tau$ , rather than the pulsating nd time,  $t$ . This transformation allows a consistent representation between the HR3BP (Eq. (19)) and HR4BP (Eq. (36)), a convenient numerical feature. To this end, from Eq. (36), substitute in  $\tau' = \frac{1}{m} \sqrt{\frac{\tilde{\mu}_S}{l_{SB*}^3}}$  in lieu of  $t'$  for Eqs. (9), (32) as well as (34). Lastly, note that the specific value for  $a_0$  defined in Eq. (5) does not change the HR4BP dynamics as it is canceled in the process of dimensionalization by Eq. (28).

### 3.4 Capabilities of QBCP and HR4BP within the Model Hierarchy

Thus far, the two coherent periodic four-body models, the QBCP and HR4BP, are cast within the common reference frame as well as common independent variable in the form of  $\vec{\rho}$ . The capabilities and limitations of these two models in bridging the gap between the CR3BP and HFEM are assessed via the coefficient functions  $b_{1-13}$  that constitute equations of motion. Then, additional insights are provided regarding the coherent solar gravity modeling in comparison with the BCR4BP and HFEM.

#### 3.4.1 Comparison of Coefficients, $b_{1-13}$

The coefficients,  $b_{1-13}$ , for the QBCP and HR4BP are plotted in Fig. 3 in comparison with the HFEM behaviors. The epoch for the QBCP and HR4BP is initialized such that the Sun-Earth-Moon is on a straight line, i.e.,  $\theta_S = \pi$ . Recall that  $\theta_S$  measures the in-plane solar position angle with respect to the pulsating-rotating frame. One epoch within the HFEM is selected on 08/27/2026 that satisfies this configuration; more information on retrieving a suitable epoch is provided in Park and Howell (2024b). The coefficients for the QBCP and HR4BP are illustrated in Figs. 3(a), 3(c), 3(e), and 3(g). The coefficients for the HR4BP are colored, whereas QBCP coefficients are plotted as white dotted lines. The corresponding HFEM coefficients are illustrated in Figs. 3(b), 3(d), 3(f), and 3(h). Caution is required in interpreting the coefficients within Fig. 3. The  $b_7$  coefficient does not appear as it is only apart from  $b_{10}$  by a very small quantity,  $b_{12} - b_{12a}$ , from Eq. (9). The last coefficient,  $b_{13}$ , is not plotted since the introduction of the pulsating nd time guarantees a fixed value, i.e., unity, for  $b_{13}$ . Also note that  $b_3/10$  is plotted instead of  $b_3$  in Fig. 3(h) for a consistent scaling with respect to the other coefficients. Moreover,  $b_5 - 2$  and  $b_{7,10} - 1$  are plotted in lieu of  $b_5$  and  $b_{7,10}$ , respectively, noting that the CR3BP supplies  $b_5 = 2$  and  $b_{7,10,13} = 1$  and zeros for the rest. Thus, the coefficients that are displayed in Fig. 3 effectively measure the perturbing accelerations in addition to the CR3BP dynamics.

In terms of the coefficients, the capabilities of the QBCP and HR4BP in bridging the CR3BP and HFEM are most apparent for  $b_{1,2}$  (Fig. 3(a) vs. Fig. 3(b)) and  $b_{7,9,10}$  (Fig. 3(e) vs. Fig. 3(f)). The first group of coefficients,  $b_{1,2}$ , are associated with the in-plane solar position components, i.e.,  $x_S, y_S$ . The second group,  $b_{7,9,10}$ , mainly originate from the frame rotation due to the in-plane solar acceleration on the Earth-Moon system. Intuitively, these components are well-approximated by the QBCP and

HR4BP that introduce the in-plane Sun with respect to the Earth-Moon pulsating-rotating frame. This observation is apparent from the fact that (1) the magnitudes of the peaks in the  $b_{7,9,10}$  coefficients are on similar levels and (2) the timing between the peaks (frequency) is similar in comparison with the HFEM. This observation is in line with previous investigations (Gómez et al., 2002; Park and Howell, 2024b), where  $\nu_2$ , the synodic frequency, is identified as the most dominant component in constituting the quasi-periodic coefficients,  $b_{1,2,7,9,10}$ .

Some limitations of the QBCP and HR4BP are visually apparent for the coefficients  $b_{4,5,12}$  (Fig. 3(c) vs. Fig. 3(d)) as well as  $b_{3,6,8,11}$  (Fig. 3(g) vs. Fig. 3(h)). For the first group,  $b_{4,5,12}$ , the magnitudes of the coefficients as modeled within the QBCP and HR4BP are significantly smaller than the HFEM behavior. Moreover, the peaks within the HFEM approximately repeat every anomalistic month ( $\nu_1$ ), whereas the synodic month ( $\nu_2$ ) governs the oscillations within the QBCP and HR4BP. Park and Howell (2024b) note that these coefficients,  $b_{4,5,12}$ , are generally associated with the Earth-Moon pulsation. As the QBCP and HR4BP introduce a nearly circular Earth-Moon distance to supply periodically forced models, they face innate challenges in accurately approximating the pulsation-related coefficients in terms of both magnitudes and frequencies. The Earth-Moon distances as modeled within the QBCP and HR4BP are plotted in Fig. 4 over one synodic month. The difference between the maximum and minimum Earth-Moon distance is less than 6,000 km for these models, whereas the HFEM produces approximately 50,000 km for the difference. The second group of coefficients,  $b_{3,6,8,11}$ , are generally associated with the out-of-plane solar position within the pulsating-rotating frame, originating from a combination of the synodic month ( $\nu_2$ ) and the draconic month ( $\nu_3$ ) indicated by Gómez et al. (2002). Thus, while the HFEM displays non-zero coefficients across different epochs, the QBCP and HR4BP always admit zeros for  $b_{3,6,8,11}$  as they assume coplanar motion for the Earth-Moon-Sun system. These innate limitations are inevitable for the periodically perturbed models, as the HFEM involves perturbations originating from multiple distinct frequencies. Thus, incorporating a single frequency implies a fundamental limitation to include perturbations associated with other types of frequencies. If the  $\nu_2$ -related perturbations govern the given dynamical regime, the QBCP and HR4BP are expected to excel in terms of bridging the gap between the CR3BP and HFEM. On the contrary, if any of the other frequencies, e.g.,  $\nu_1$  or  $\nu_3$ , produces non-negligible impact, the QBCP and HR4BP are expected to face challenges in approximating the higher-fidelity gravitational environment.

The similarities and differences between the QBCP and HR4BP are noted. From Fig. 3, it is obvious that the two models produce extremely similar behaviors across the time over one year, alluding to a global similarity across cislunar space. This observation complements the previous investigations that focus on specific domains to illustrate the similarity between the two models, for example, the vicinity of the  $L_2$  Lagrange point as discussed in Andreu (1998); Rosales et al. (2023); Peterson et al. (2023); Henry et al. (2023). The similarity is also apparent from the Earth-Moon distance plots in Fig. 4, resulting in similar coefficients that derive from the Earth-Moon distance. While in general, the QBCP and HR4BP are expected to behave similarly,

the most notable difference is the fundamental frequencies that govern the periodicity for these models. From Fig. 4, the QBCP is periodic over one synodic period. In contrast, the HR4BP is periodic over one half of the synodic period. This discrepancy results from the Hill approximation (Eq. (31)) employed in deriving the HR4BP dynamics. Physically, the HR4BP treats two Sun angles apart by  $\pi$  equivalently; this equivalence is also observed from Eq. (16) where  $2\theta_S$  appears in the expression. Thus, the HR4BP is essentially a variation of the QBCP with the Hill approximation that results in an additional symmetry. This aspect potentially allows the HR4BP to admit more available patterns. The perpendicular crossing, a sufficient condition to admit a periodic orbit for the spacecraft motion (Sanaga and Howell, 2023), occurs at both the minimum and maximum Earth-Moon distances within the HR4BP, i.e., at  $(0, 1/4, 1/2, 3/4, 1)$  times the synodic period; however, for the QBCP, such configuration only occurs at the minimum Earth-Moon distances at  $(0, 1/2, 1)$  times the synodic period from Fig. 4. Due to the additional approximation that is present within the HR4BP, however, some perturbations are not as accurately modeled within the HR4BP as opposed to the QBCP. As the HR4BP is doubly periodic over one synodic month, the fundamental frequency is  $2\nu_2$ , as opposed to  $\nu_2$  for the QBCP. For some quasi-periodic coefficient behavior from the HFEM, the QBCP is capable of introducing perturbations in the form of *multiples* of  $\nu_2$ , i.e.,  $\nu_2, 2\nu_2, 3\nu_2, \dots$ . However, the HR4BP faces challenges in modeling the *odd* multiples of  $\nu_2$ ; this challenge originates from the fact that the HR4BP does not differentiate  $\theta_S$  from  $\theta_S + \pi$ . Typically, the HFEM perturbations introduce only small perturbations in terms of the odd multiples of  $\nu_2$  (Gómez et al., 2002; Lian et al., 2013; Park and Howell, 2023) and, thus, the two coherent four-body problems behave qualitatively similarly. In Section 5, an opposite case is revealed where the odd multiples of  $\nu_2$  indeed matter, and QBCP and HFEM produce qualitatively different behaviors.

### 3.4.2 Solar Gravity: Coherent Representation

The *coherent* four-body models, QBCP and HR4BP, result in a common cancellation for a subset of terms in the dynamics represented by  $\ddot{\rho}_{Solar,G}$  from Eq. (13). The expression approximately displays the behavior as described by Eq. (15). The visual interpretation for such expression is available in Park and Howell (2024b), where different points within the pulsating-rotating frame are sampled and the corresponding accelerations for  $\ddot{\rho}_{Solar,G}$  are examined while assuming  $z = 0, z_S = 0$ . The resulting contour plots are included in Fig. 5. Figures 5(a) and 5(b) illustrate the behaviors for the BCR4BP and HFEM for comparison, regenerated from Park and Howell (2024b). Ranges between  $-1.2 < x < 1.2$  and  $-1.2 < y < 1.2$  that encompass cislunar space are investigated in the plots for a sample epoch on 09/23/2023. The white circles and red x's denote the Earth and Moon, and the five Lagrange points, respectively. The colors denote the non-dimensional acceleration magnitude at each point, and the cyan arrows illustrate the corresponding acceleration direction. It is apparent that the coherent representation of the solar gravity as modeled within the QBCP, HR4BP, and the HFEM reflect the patterns from Eq. (16) and dominate the global behavior for  $\ddot{\rho}_{Solar,G}$ . In contrast, the BCR4BP, a model that lacks the coherency in modeling the solar gravity, does not produce a similar pattern. Thus, it is expected that



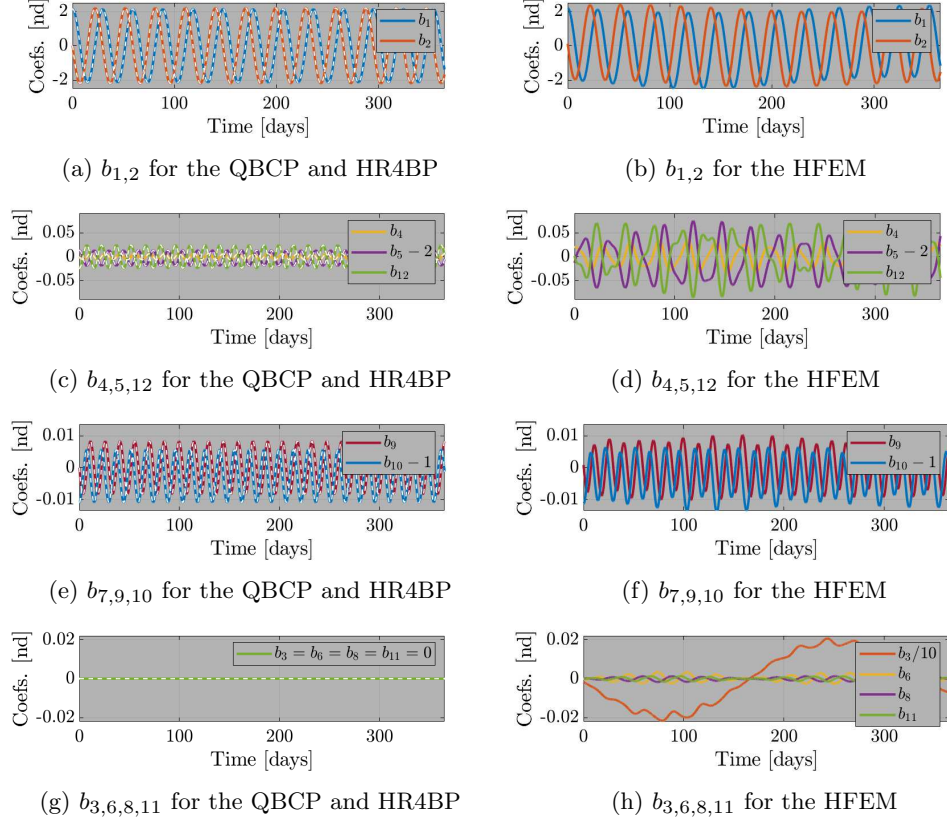


**Fig. 3:** Coefficient for the QBCP (white dotted lines) and HR4BP in comparison with HFEM starting on 08/27/2026

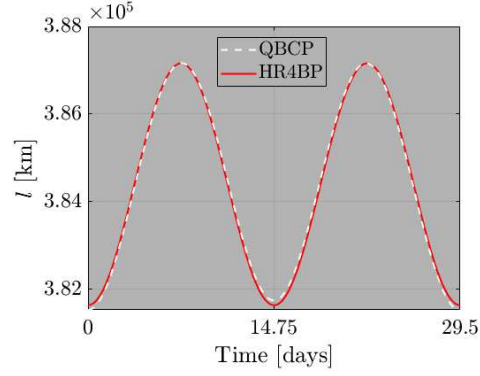


**Fig. 4:** Earth-Moon distance ( $l$ ) in the QBCP and HR4BP over one synodic month

the coherent representation for the solar gravity that results in the patterns governed by Eq. (16) is a key component in properly approximating the HFEM across cislunar space, a point of consideration for constructing a suitable hierarchy of dynamical models within cislunar space.

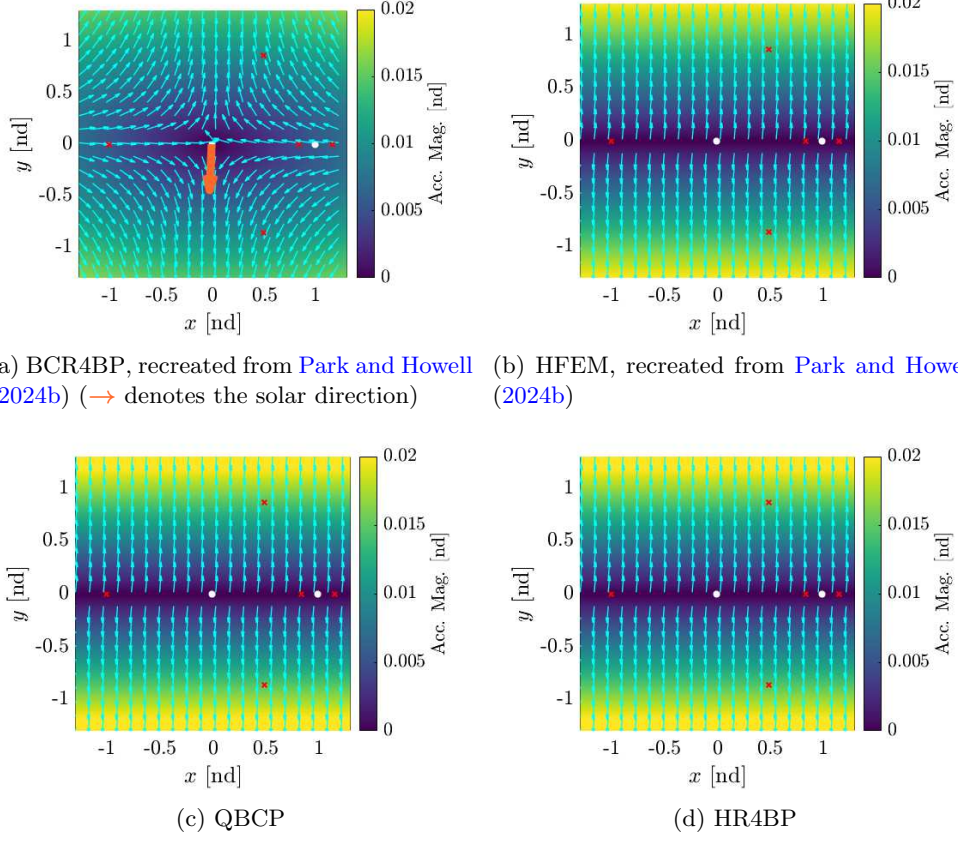


**Fig. 5:** Solar gravity acceleration ( $\ddot{\rho}_{Solar,G}$ ) pattern on 09/23/2023

## 4 Quasi-Periodically Perturbed Models: Quasi-Hill Restricted Four-Body Problem (QHR4BP)

A natural extension to the periodically forced models is achieved by including two frequencies simultaneously, resulting in a quasi-periodically perturbed model. Within the model hierarchy as illustrated in Fig. 1, it is likely that these quasi-periodically perturbed models better approximate HFEM by more accurately representing the

quasi-periodic nature of the coefficients,  $b_{1-13}$ , within the pulsating-rotating formulation. In the previous section, potential limitations of the periodically perturbed four-body models, i.e., the QBCP and HR4BP, are visualized in terms of  $\nu_1$ -related coefficients ( $b_{4,5,12}$ ) and  $\nu_3$ -related coefficients ( $b_{3,6,8,11}$ ). These challenges are mitigated via incorporating  $\nu_1$  or  $\nu_3$  into the existing  $\nu_2$ -related dynamical models. Note that multiple examples exist from previous literature (Assadian and Pourtakdoust, 2010; Villegas-Pinto et al., 2023; Kelly et al., 2023) that introduce quasi-periodically perturbed models. However, these models generally lack coherency for the solar gravity modeling, where the Earth-Moon motion remains Keplerian even in the presence of the solar gravity. This assumption likely results in limitations for approximating the solar gravity induced acceleration that demonstrates the pattern that appears in Eq. (16) as well as Fig. 5. Thus, one key challenge in constructing a quasi-periodically perturbed model within the Earth-Moon system is to guarantee coherency, while incorporating two frequencies in addition to the CR3BP.

In the current analysis, the insights from Hill’s lunar theory as well as modern dynamical systems theory are leveraged to suitably design coherent quasi-periodically perturbed models. Within the formulation for the HR4BP introduced by Scheeres (1998), the Earth-Moon motion is represented as the lunar variational (variation) orbit, a periodic orbit within the HR3BP that is originally introduced by Hill (1878). While the periodicity of the variational orbit results in the periodic force for the HR4BP within Earth-Moon rotating frames, note that any particular solutions from the HR3BP may be leveraged to represent the Earth-Moon motion in the presence of the Sun, deemed to be a coherent representation of the solar gravity. In the following sections, the lunar variational orbit originally introduced by Hill (1878) is reviewed. Then, utilizing modern dynamical systems theory, the linear stability characteristics of the variational orbit are examined, locating linear center subspaces. Then, two distinct nonlinear center manifolds that evolve from the underlying variational periodic orbit are investigated, each providing two-dimensional (2D) Quasi-Periodic Orbits (QPOs). These particular solutions are then leveraged to extend the HR4BP to two quasi-periodically forced models [Goal (G3) from Section 1.1] denoted the In-plane Quasi-Hill Restricted Four-Body Problem (I-QHR4BP) and Out-of-plane Quasi-Hill Restricted Four-Body Problem (O-QHR4BP).

#### 4.1 Lunar Variational Orbit in the HR3BP

The HR3BP describes the motion of a massless body that is under the gravitational influence of two primaries, one of which is significantly more massive than the second one (Hill, 1878; Szebehely, 1967). Hill (1878) initially develops the HR3BP in his lunar theory to supply an approximate solution for the lunar motion. The two primaries in this case are the Sun and the Earth. He selects the variational (variation) orbit, one particular member along the family “ $g$ ” within the HR3BP (Hill, 1878; Hénon, 1969), as such solution. In Fig. 6, a subset of the family  $g$  is plotted. Note that the origin is at the smaller primary, the Earth. Family  $g$  is a one-parameter family, where it approximates a circular orbit in the vicinity of the Earth but progressively becomes more oval as it extends in the configuration space as illustrated in Fig. 6(a). In Fig. 6(a), the orbits are colored with respect to their period values measured in  $m\tau$  nd units;

such a time unit is typically employed for the HR3BP. The black orbit in Fig. 6(a) corresponds to the variational orbit describing the Earth-Moon motion within the Sun-Earth-Moon HR4BP (Scheeres (1998)), with a period that tracks the synodic lunar month. The synodic period is denoted as  $P_2$  in the current investigation, associated with the frequency of  $\nu_2$ . Note that the values correspond to 29.528 days,  $2\pi(1+m)$ ,  $2\pi$ , and  $2m\pi \approx 0.5080$  in  $T$ ,  $t_*$ ,  $\tau$ , and  $m\tau$ , respectively. In Fig. 6(b), the period is plotted as a function of  $\xi_0$ , the location on the  $\hat{i}_H$ -axis with  $\xi > 0$  for reference.

The linear stability information for the variational orbit (black in Fig. 6(a)) is analyzed. As the HR3BP is an autonomous Hamiltonian system, the monodromy matrix for the periodic orbit supplies three pairs of *reciprocal* eigenvalues (Meyer and Offin, 2018) as: (i) 1, 1, (ii)  $\approx 0.9005 \pm 0.4348j$ , and (iii)  $\approx 0.8601 \pm 0.5100j$ , where  $j$  is the imaginary number in the complex pairs. Note that the first trivial pair denotes the existence of family of periodic orbits, i.e., family  $g$ . The other two pairs allow linear center subspaces with the rotation numbers, or, the angles between the imaginary and real parts of the eigenvalues, that is,

$$\sigma_1 \approx \arctan\left(\frac{0.4348}{0.9005}\right) \approx 25.7700^\circ, \quad \sigma_3 \approx \arctan\left(\frac{0.5100}{0.8601}\right) \approx 30.6617^\circ \quad (39)$$

where subscripts 1 and 3 denote the two directions with the in-plane eigenvector (1) and out-of-plane eigenvector (3). The dimensional periods associated with the oscillatory behaviors within the linear center subspaces are,

$$P_1 = \frac{2\pi P_2}{2\pi + \sigma_1} \approx 27.5562 \text{ days}, \quad P_3 = \frac{2\pi P_2}{2\pi + \sigma_3} \approx 27.2112 \text{ days}. \quad (40)$$

It is significant that the periods  $P_1, P_3$  are numerically close to the anomalistic and draconic periods associated with the frequencies  $\nu_1 = 2\pi/P_1$  and  $\nu_3 = 2\pi/P_3$ , respectively. These observations are also made in Aydin (2023).

## 4.2 Nonlinear QPOs in the Vicinity of the Lunar Variational Orbit

The linear center subspaces that exist for the lunar variational orbit within the HR3BP each allows a nonlinear center manifold that is tangent to the linear center subspace. These nonlinear center manifolds are associated with 2D-QPOs that are diffeomorphic to 2D-tori. In general, the spacecraft state on a 2D-QPO is represented by two angular variables,  $\theta_{lon}$  and  $\theta_{lat} \in [0, 2\pi)$ , denoted as the longitudinal and latitudinal angles. These angles flow linearly with an independent variable with respective frequencies denoted as  $\nu_{lon}$  and  $\nu_{lat}$ . While multiple numerical schemes exist to approximate the two-dimensional QPO structures, in the current work, an algorithm developed by Gómez and Mondelo (2001) as well as Olikara and Scheeres (2012) (GMOS) is leveraged. In the algorithm, the invariant curve is defined as a closed curve parameterized by  $\theta_{lat}$  for a fixed  $\theta_{lon}$  value. Then, after one longitudinal period, the trajectory that starts on the invariant curve remains on the same curve, but rotates by a fixed angle in  $\theta_{lat}$ . This rotation angle is computed as  $\sigma = \text{mod}(2\pi\nu_{lat}/\nu_{lon}, 2\pi)$ , where

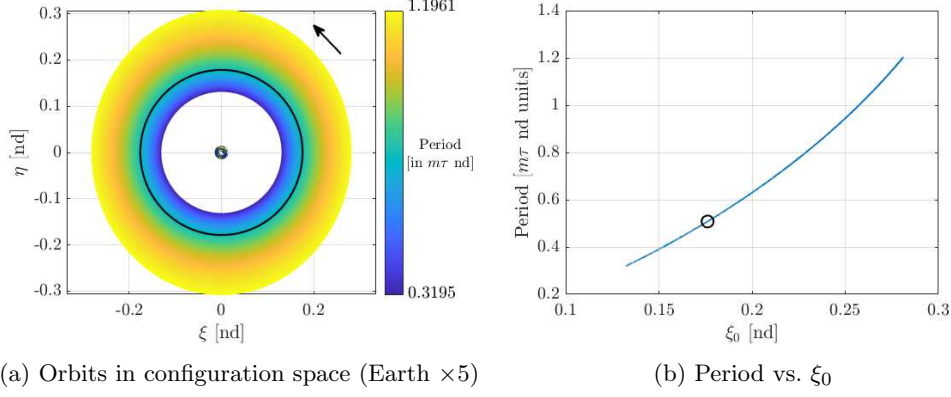


**Fig. 6:** A subset of family  $g$  from the HR3BP. Black corresponds to the orbit representing the Earth-Moon motion in the HR4BP

“mod” denotes the modular operator. Utilizing this *invariance condition*, the GMOS algorithm numerically locates the invariant curve approximated by discrete sample points leveraging the Discrete Fourier Transform (DFT). For more information on the numerical implementation of the GMOS algorithm, refer to Appendix B.

In general, 2D-QPOs within the HR3BP exist as two-parameter families. Multiple combinations of two variables exist to describe the evolution of the 2D-QPO and the two frequencies,  $\nu_{lon}$  and  $\nu_{lat}$ , serve as such a combination. In the current analysis, the longitudinal frequency is associated with the orbit period, i.e.,  $\nu_{lon} = \nu_2 = 2\pi/P_2$  and  $\theta_{lon} = \theta_2 = \nu_2\tau$ . This frequency value is assumed to be fixed to accurately track the synodic month, i.e., the underlying period  $P_2$  does not change, also a common practice within Hill’s lunar theory (Gutzwiller, 1998). Then, the 2D-QPOs in the current analysis are described as one-parameter families that evolve with the other frequency,  $\theta_{lat}$ . From the eigenstructure analysis, two different families of 2D-QPOs exist within the in-plane ( $\hat{i}_H - \hat{j}_H$ ) direction as well as the out-of-plane ( $\hat{k}_H$ ) direction. The latitudinal frequencies for these two families generally track  $\nu_1$  and  $\nu_3$ , where the linear estimates from Eq. (40) evolve in a nonlinear fashion along each direction.

#### 4.2.1 In-Plane 2D-QPO Family: Introduction of Eccentricity

The in-plane 2D-QPO family characteristics are examined and a particular member is selected to mirror the realistic Earth-Moon system. Sample invariant curves along the in-plane HR3BP QPO originating from the lunar variation PO are illustrated in Fig. 7(a) within the position space. For construction of the invariant curve,  $\theta_2 = 0$  is leveraged, defined such that the average  $\eta$  value for the invariant curve is zero with  $\xi > 0$ . It is notable that this family originates from the underlying PO and the invariant curve expands in size within the  $\hat{i}_H - \hat{j}_H$  plane, where the lunar variational PO is observed as a fixed point in Fig. 7(a). However, the  $\hat{k}_H$ -component ( $\zeta$ ) for the orbit remains zero and the Earth-Moon-Sun system is still coplanar. An alternative representation of the one-parameter QPO family is available in Fig. 7(b). The vertical

axis illustrates the ratio of the latitudinal frequency,  $\nu_{lat} = \nu_1$ , to the longitudinal frequency,  $\nu_{lon} = \nu_2$ . Note that the value remains above unity, implying that the anomalistic month ( $\approx 27.56$  days), associated with  $\nu_1$ , is always shorter lunar synodic month associated with  $\nu_2$ . While the ratio monotonically increases from the linear value, the variation is considered marginal, i.e., in terms of frequency, such that any member along the 2D-QPO family is able to introduce a suitable  $\nu_1$  value that accurately tracks the realistic HFEM value. The horizontal axis of Fig. 7(b) illustrates the approximate eccentricity for the lunar orbit with respect to the Earth,  $e_a$ . The value is evaluated as,

$$e_a = \frac{\xi_{max}(\theta_2 = 0) - \xi_{min}(\theta_2 = 0)}{(15m/4 + 2)A_0}, \quad (41)$$

leveraging the insights from Hill’s lunar theory (Darwin, 2009/1916), further detailed in Appendix C. Recall that  $m \approx 0.0808$  and  $A_0$  is computed as  $A_0 = a_0(1 - m^2/6)$  with  $a_0$  from Eq. (5). At the reference invariant curve,  $\theta_2 = 0$ , the  $\xi_{max,min}$  denote the maximum and minimum  $\xi$  values. Of course, note that a true “eccentricity” does not exist to describe the QPO family in the presence of the solar gravity since the Earth-Moon system does not remain Keplerian;  $e_a$  serves as a reference value to approximately represent the eccentricity. One particular member along the family is plotted in red in Fig. 7(a), corresponding to a reasonable value that approximates the realistic Earth-Moon eccentricity,  $e_a \approx 0.055$ ; for reference, Brown (1896) selects  $e_a \approx 0.0548993$  based on observational data. The selected invariant curve is illustrated in Fig. 8, where 25 initial conditions along the invariant curves are propagated for one synodic month within the HR3BP. Any initial condition that is located on this two-dimensional in-plane QPO is bounded on the same structure, indefinitely within the HR3BP. Note that the illustrated QPO family extends beyond the plotted values; however, such QPOs lose physical significance within the Earth-Moon-Sun system due to excessively large eccentricity values,  $e_a$ .

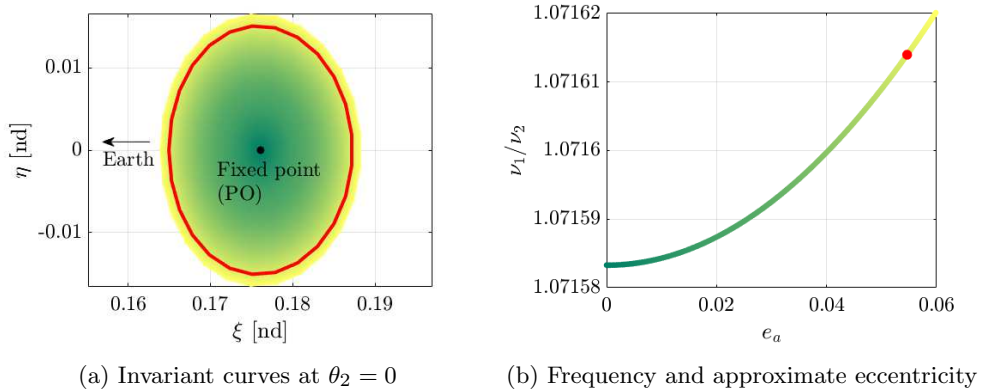
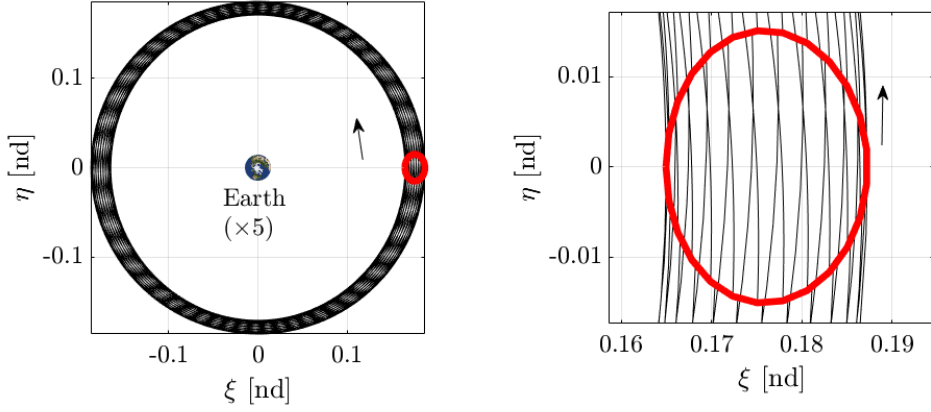


**Fig. 7:** In-plane QPO family





(a) Selected QPO and the invariant curve

(b) Zoomed-in view near  $\theta_2 = 0$

**Fig. 8:** Selected member along the in-plane QPO family

#### 4.2.2 Out-of-Plane 2D-QPO Family: Introduction of Inclination

The out-of-plane QPOs' characteristics are also examined and a suitable sample member is selected to realistically model the Earth-Moon system. Utilizing the GMOS algorithm, the nonlinear QPOs that primarily evolve in the out-of-plane direction,  $\hat{k}_H$ , are constructed and sample invariant curves are illustrated in Fig. 9(a) and observed in position space. The latitudinal frequency for the family is denoted as  $\nu_3$ , where the ratio of  $\nu_3$  to the synodic frequency,  $\nu_2$ , is plotted in Fig. 9(b). Again, the ratio remains above unity, tracking the draconic month that remains shorter than the synodic month as well as the anomalistic month. The horizontal axis in Fig. 9(b) illustrates the approximate inclination of the lunar orbit with respect to the Earth ecliptic plane. From the linear analysis in Darwin (2009/1916), the value is approximately,

$$i_a = \arctan \left( \frac{\zeta_{max}(\theta_2 = 0) - \zeta_{min}(\theta_2 = 0)}{(-3m/4 + 2)A_0} \right), \quad (42)$$

where  $\zeta_{max,min}$  values are defined along the invariant curve constructed at  $\theta_2 = 0$ , illustrated in Fig. 9(a). In the HFEM, the realistic Earth-Moon-Sun system admits a value of  $i_a \approx 5^\circ$ . For reference, Brown (1896) selects  $i_a \approx 5.14363^\circ$ . One sample member near this inclination value is depicted in red within Fig. 9, where the corresponding QPO is plotted in Fig. 10 in position space.

#### 4.2.3 Remarks on Hill's Lunar Theory

Many insights in the current section (Section 4) originate from Hill's original work on the lunar theory. In review of Hill's lunar theory, Gutzwiller (1998) observes that the linear center subspaces for the lunar variational orbit within the HR3BP imply a

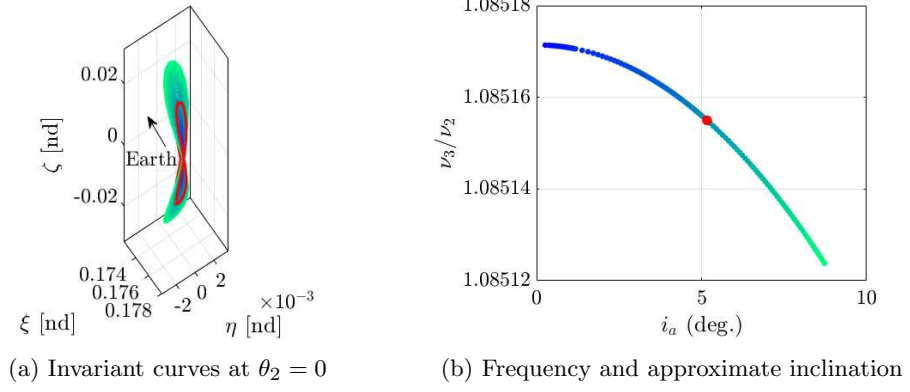


**Fig. 9:** Out-of-plane QPO family

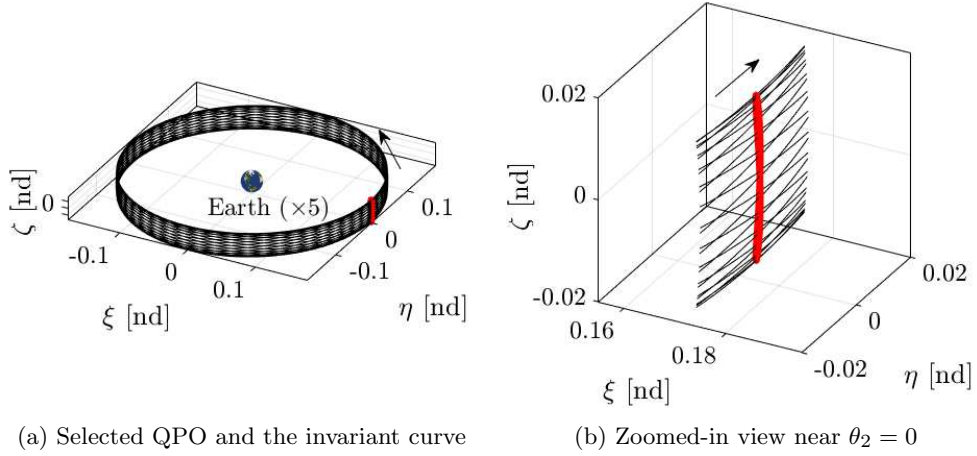


**Fig. 10:** Selected member along the out-of-plane QPO family

three-dimensional QPO representation of the lunar motion around the Earth. In the current work, it is demonstrated that modern computational and dynamical systems theory tools can be leveraged to construct nonlinear 2D-QPO structures within the HR3BP that *selectively* introduce perturbations with distinct frequency information; the in-plane QPOs introduce  $\nu_{1,2}$  and the out-of-plane QPOs introduce  $\nu_{2,3}$ . Note that the latitudinal frequency evolution, i.e.,  $\nu_{1,3}$ , along the QPO families remain marginal for the realistic range of  $e_a, i_a$ , where the linearly approximated frequencies serve as reasonable estimates. This aspect partly explains the huge success of analytical lunar theories that rely heavily on the frequency information derived from the linear analysis on the underlying variational PO. Lastly, recall that the HFEM is approximated with five different frequencies as pointed out in [Gómez et al. \(2002\)](#). The QPO analysis



within the HR3BP is able to generate first three frequencies out of five. The other two are generally associated with the Earth’s eccentricity around the Sun (assumed to be zero within the HR3BP) and the sidereal lunar month (Gómez et al., 2002).

### 4.3 Designing QHR4BP Models

The 2D-QPOs within the HR3BP are leveraged to construct a range of quasi-periodically perturbed models. Note that the HR4BP formulation originally introduced by Scheeres (1998) incorporates *any* particular solution from the HR3BP. For a variational PO, the periodically forced HR4BP is designed. In the current investigation, the HR3BP QPOs as illustrated in Figs. 8(a) and 10(a) are leveraged as particular solutions within the HR4BP formulation to supply various quasi-periodically perturbed HR4BPs. From the in-plane QPO, the In-plane Quasi-Hill Restricted Four-Body Problem (I-QHR4BP) is designed that introduces two frequencies,  $\nu_{1,2}$ . From the out-of-plane QPO, the Out-of-plane Quasi-Hill Restricted Four-Body Problem (O-QHR4BP) is constructed with two frequencies,  $\nu_{2,3}$ .

For the formulation of these QHR4BPs, the equations of motion as designed within the pulsating-rotating frame in the form of Eqs. (8) and (36) are leveraged. Note that the original derivation of HR4BP by Scheeres (1998) leverages the uniform-rotating frame (Fig. 2(b)), where the Earth and the Moon are not fixed. For the lunar variational PO, the change in the Earth-Moon distance is relatively small such that the uniform-rotating frame serves as a suitable reference frame. In contrast, for the QPOs as introduced in Figs. 8(a) and 10(a), the lunar motion displays more significant deviations in general. Figure 11 illustrates this behavior, where the lunar motion as described by the variational PO from Fig. 6(a) and the selected in-plane QPO are plotted in the uniform-rotating frame illustrated in dimensional units. In contrast to the PO, the in-plane QPO demonstrates a notable deviation for the lunar motion within the frame. Trajectories generated within this frame potentially lose some physical intuition as the Moon is significantly moving. Also, for the orbits in the vicinity of the Moon, the numerical targeting process potentially faces some extra sensitivity issues, forced to target with respect to a moving body, the Moon. Thus, although it is possible and clearly useful to derive the equations of motion within the uniform-rotating frame following the procedure in Scheeres (1998), the current investigation designs the QHR4BPs within the pulsating-rotating frame.

The form of the equations of motion for the QHR4BPs remains identical to Eq. (36). The only differences manifest in evaluating the coefficients,  $b_{1-13}$ , where the quantities that characterize the Earth-Moon system are leveraged, e.g.,  $l$ ,  $h$ ,  $\vec{V}_{EM}$ , from Eqs. (28)-(30). For the HR4BP that leverages the HR3BP PO, these quantities are derived from Fourier series governed by one frequency,  $\nu_2$ . While it is possible to extend this approach to represent the HR3BP QPOs as 2D Fourier series formulated with two frequencies, the current investigation leverages a numerical approach. Without losing generality, focus on the I-QHR4BP modeling  $\nu_{1,2}$ . Assume that, at the initial epoch,  $\tau = \tau_0$ , the Moon originates on the invariant curve at  $\theta_1 = \theta_2 = 0$  with the initial position and velocity vectors as  $\vec{r}_{EM,0}$  and  $\dot{\vec{r}}_{EM,0}$ , respectively. Then, at  $\tau = \tau_F$ ,  $\theta_{1-2} = \nu_{1-2} \cdot (\tau_F - \tau_0)$  and  $\vec{r}_{EM,F}$  and  $\dot{\vec{r}}_{EM,F}$  are constructed via numerically integrating the HR3BP dynamics in Eq. (19) from  $\tau_0$  to  $\tau_F$  with the initial condition.

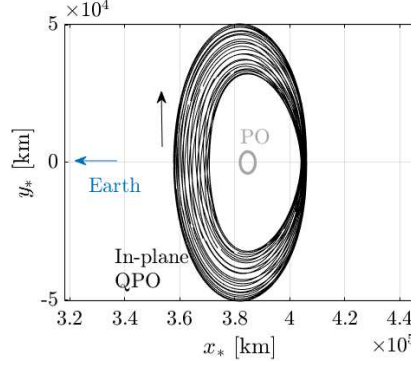


**Fig. 11:** Lunar variational PO and the selected in-plane QPO within the uniform-rotating frame

Thus, for each instance, the lunar motion within the HR3BP is *numerically* evaluated to supply coefficients  $b_{1-13}$  via the process described in Section 3.3. The I-QHR4BP and O-QHR4BP leverage the in-plane and out-of-plane Quasi-Periodic Orbit (QPO) initial conditions for the lunar motion, respectively.

#### 4.4 QHR4BPs: Coefficient Analysis

The selected invariant curves in Figs. 7(a) and 9(a) are leveraged to supply the suitable I-QHR4BP and O-QHR4BP model that *better* approximate the HFEM behavior. The global capabilities for these quasi-periodically perturbed models are illustrated in terms of the coefficients,  $b_{1-13}$ . Recall that the HFEM supplies complex behaviors for the coefficients governed by multiple frequencies. In Section 3 and Fig. 3, it is illustrated that the QBCP and HR4BP face challenges in modeling  $\nu_1$ -dominated coefficients ( $b_{4,5,12}$ ), and  $\nu_3$ -dominated coefficients ( $b_{3,6,8,11}$ ). It is expected that the newly introduced QHR4BPs excel in modeling these coefficients by introducing either  $\nu_1$  or  $\nu_3$  in addition to  $\nu_2$ .

The coefficients for the I-QHR4BP and O-QHR4BP are plotted in Fig. 12 over one year. The left and right columns illustrate the behaviors for the I-QHR4BP and O-QHR4BP, respectively. Recall that the corresponding data for the HFEM is included in Fig. 3. For the reference HFEM initial epoch on 08/27/2026, the corresponding initial epoch for the QHR4BPs are computed in terms of  $\theta_{1-3}$ . As these quasi-periodically perturbed models both incorporate the  $\nu_2$ -related information, the capabilities in modeling  $b_{1,2}$  as well as  $b_{7,9,10}$  remain similar to those from QBCP and HR4BP. Additionally, it is notable that the I-QHR4BP indeed succeeds in estimating the  $b_{4,5,12}$ , a group of coefficients governed by  $\nu_1$  (Fig. 12(c) vs. Fig. 3(d)). However, as the I-QHR4BP still assumes a coplanar motion for the Earth-Moon-Sun system, it produces zero estimates for the other group,  $b_{3,6,8,11}$ . These coefficients are better approximated within the O-QHR4BP that introduces the inclination of the lunar orbit with respect to the Earth ecliptic plane. Comparing Fig. 12(h) and Fig. 3(h), it is apparent that the O-QHR4BP excels in modeling the  $\nu_3$ -related perturbations in

comparison with the HFEM. Note, however, that  $b_{4,5,12}$  coefficients are not successfully modeled within the O-QHR4BP. The Earth-Moon distance as modeled within various models is plotted in Fig. 13 to offer additional insights. As opposed to the HR4BP, the I-QHR4BP introduces significantly more accurate Earth-Moon distance behavior compared to the HFEM; a trait achieved via selecting an invariant curve with a desired approximate eccentricity value,  $e_a$ . However, for the O-QHR4BP, the Earth-Moon distance behavior remains similar to the HR4BP, as the main information that the model introduces is in the  $\hat{k}_H$ -direction that results in a non-zero  $i_a$  value. Thus, to incorporate perturbations originating from three different frequencies at the same time, a three-dimensional QPO within the HR3BP is required that remains beyond the current scope. Also, such a step is often not required if any of the intermediate models introducing a fewer number of frequencies is deemed sufficient. Within the model hierarchy as described in Fig. 1, it is desired to leverage the I-QHR4BP and O-QHR4BP for regions where either  $\nu_{1,2}$  or  $\nu_{2,3}$ -related perturbations are both non-negligible, respectively, serving as suitable extensions to the existing periodically perturbed models within the hierarchy that can be selectively employed.

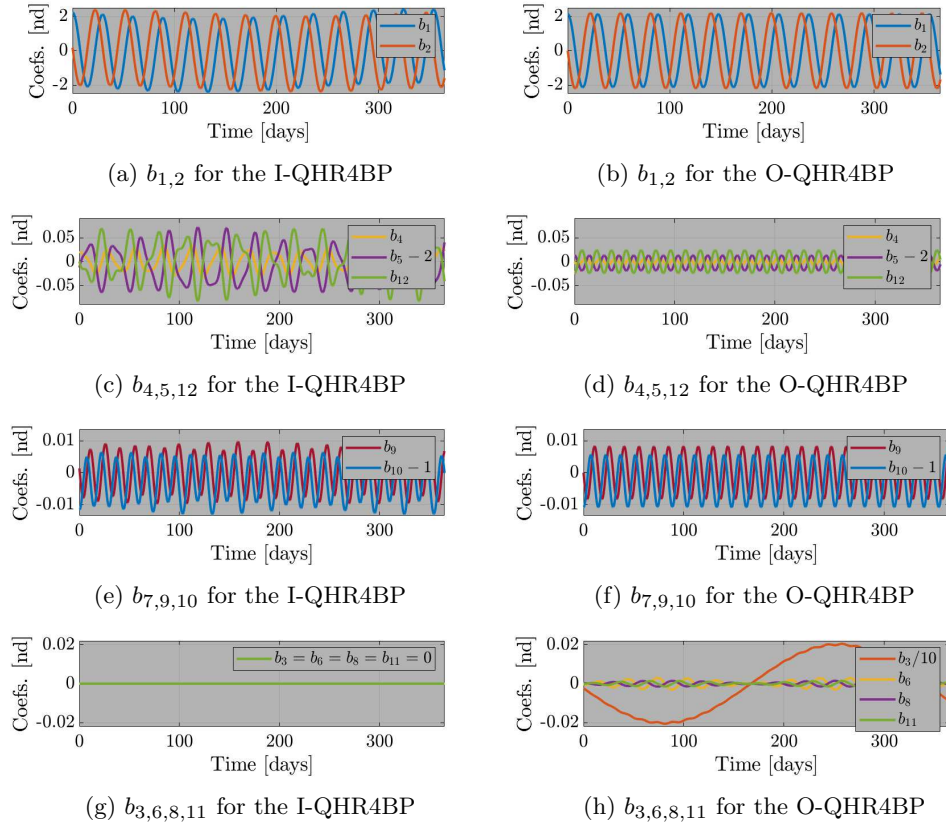


**Fig. 12:** Coefficient for the QHR4BPs (compare with the HFEM coefficients in Fig. 3)

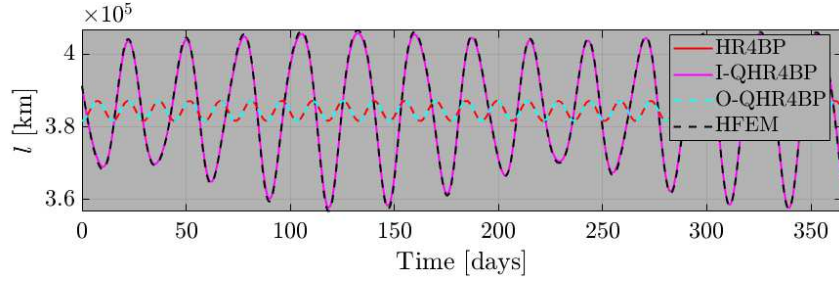


**Fig. 13:** Earth-Moon distance ( $l$ ) in the HR4BP, QHR4BPs and HFEM

## 5 Applications

Noting that the three main objectives of the current investigation are completed [Goals (G1)-(G3) from Section 1.1] thus far, the insights gained for the (quasi-) periodically perturbed models are examined for sample applications where the CR3BP structures are transitioned to the HFEM analogs. Then, the behaviors of the counterparts that exist within various intermediate models are compared to assess the capabilities and limitations of the models within the context of the model hierarchy. Preliminary information is reviewed for the evolution of the CR3BP structures to (quasi-) periodically perturbed model counterparts. Then, two sample applications are discussed for the Earth-Moon  $L_2$  Lagrange point and the  $L_2$  9:2 synodic resonant halo orbit.

### 5.1 Evolution of the CR3BP structures

The evolution of the CR3BP structures to the (quasi-) periodically perturbed models are characterized by the number of frequencies required to represent a given structure. Generally, for the CR3BP structures governed by  $n$  frequencies, the periodic and quasi-periodic perturbations lead to counterparts with  $n + 1$  and  $n + 2$  frequencies, respectively. The extra frequencies are inherited from the model frequency itself (Jorba and Villanueva, 1997). Thus, for a sample CR3BP PO governed by one frequency,  $\nu_C$ , the corresponding counterparts within the periodically forced models result in 2D-QPOs governed by  $\nu_C$  and the other frequency, e.g.,  $\nu_2$ . Similarly, the quasi-periodically perturbed models supply three-dimensional QPOs governed by  $\nu_C$  as well as the other two frequencies innate to the model. In general, however, three-dimensional QPOs are more challenging to construct as opposed to the lower-dimensional structures. The reduction in the number of frequencies is possible for resonant cases, i.e., the frequency of the CR3BP PO,  $\nu_C$ , is in an integer ratio to any of the model frequencies,  $\nu_i$ , ( $1 \leq i \leq 5$ ). The current analysis focuses on structures that are described via maximum of 2 frequencies leveraging the resonant properties.

The numerical process for delivering the structures within periodically forced models that emanate from the CR3BP POs are well-documented in literature for various models. For a case where  $\nu_C$  is in resonance with the model frequencies, examples are provided in Boudad et al. (2020); Brown et al. (2024); Peng and Xu (2015); Ferrari

and Lavagna (2018); Sanaga and Howell (2024); Andreu (1998) that discuss *resonant* POs within periodically forced models including the ER3BP, BCR4BP, HR4BP, and QBCP. For a case where  $\nu_C$  is not commensurate with the model frequency, 2D-QPOs are determined within various models in Park and Howell (2024a); Rosales et al. (2023); Henry et al. (2023); Rosales et al. (2021). The results within this section leverage the numerical processes investigated by these previous authors. While the literature for constructing 2D-QPOs within quasi-periodically perturbed models is more scarce, the process remains similar to computing 2D-QPOs within the periodically perturbed models. One notable example is provided in Villegas-Pinto et al. (2023), where a 2D-QPO is successfully produced within a quasi-periodically perturbed model. Another example appears in Kelly et al. (2023) as well. For illustration, assume that the investigated model is the I-QHR4BP, governed by  $\nu_{1,2}$ . Without losing generality, also assume that  $\nu_2$  is in resonance with  $\nu_C$  such that a ratio exists,  $\nu_C : \nu_2 = p : q$ , where  $p, q$  are coprime integers. Then, the GMOS QPO computation algorithm is constructed with a stroboscopic time of  $qP_2$  such that full cycles in  $\nu_2$  as well as  $\nu_C$  are completed. Then, at the stroboscopic map, the invariance condition as discussed in Appendix B is applied with the rotation angle  $\sigma = \text{mod}(\nu_1 q P_2, 2\pi)$  via the latitudinal frequency,  $\nu_1$ . Often, the desired counterparts within the QHR4BP are far from the original CR3BP structure. In such a case, a numerical continuation process aids in gradually increasing the perturbations in both frequency directions. In the current analysis, it is assumed to continue first along the  $\nu_2$ -direction. This step is identical to the continuation process from the CR3BP to HR4BP as detailed in Sanaga and Howell (2024); Henry et al. (2023); Brown et al. (2024), where the parameter  $m$  serves as a continuation parameter between 0 (CR3BP) and  $\approx 0.0808$  (HR4BP). Upon reaching the HR4BP, the second continuation direction is along the invariant curves as displayed in Figs. 7(a) and 9(a). Perturbations in  $\nu_{1,3}$ -directions are gradually increased by stepping along the respective members within the HR3BP QPO families. Note that this process is a *natural parameter* continuation, where the parameters are considered to be  $e_a$  and  $i_a$  as appear within Figs. 7(b) and 9(b), respectively. The continuation process ends upon reaching the desired values corresponding to the orbits described in 8(a) and 10(a). At this point, the 2D-QPOs within the QHR4BPs are successfully achieved. In the current investigation, 100 steps are required between the HR4BP and the QHR4BPs.

## 5.2 $L_2$ Lagrange Point

The evolution of five Lagrange equilibrium points from the Earth-Moon CR3BP to the HFEM includes various theoretical and practical implications. Theoretically, of course, the evolution of the equilibrium points represents one of the simplest scenarios, serving as an initial step for understanding the evolution of other multi-body dynamical structures. Also, the  $L_1$  and  $L_2$  points are crucial in characterizing the global transit properties in and out of the Earth-Moon system; the evolution of such behavior is crucial in understanding the realistic properties within the HFEM as well.

The current investigation focuses on the  $L_2$  point, given the relevant previous research. The  $L_2$  equilibrium point displays diverse behaviors when transitioned to periodically forced models as well as the HFEM. In characterizing the evolution, the

selection of the frame has profound impact on the results. Within the pulsating-rotating frame, it is trivially demonstrated that the ER3BP also admits an equilibrium  $L_2$  point (to observe this, refer to [Park and Howell \(2024b\)](#)). Within the QBCP, the  $L_2$  point evolves to a PO with three distinct lobes as determined within the pulsating-rotating frame and discussed in [Andreu \(1998\)](#); [Jorba-Cuscó et al. \(2018\)](#); [Rosales et al. \(2023\)](#). The HR4BP's  $L_2$  counterpart also displays a periodic motion, but represented within the uniform-rotating frame as discussed in [Olikara et al. \(2016\)](#); [Henry et al. \(2023\)](#); [Peterson et al. \(2023\)](#). However, the HR4BP's  $L_2$  counterpart behavior within the pulsating-rotating frame does not appear in literature at least from the efforts of the authors. Within the BCR4BP, a suitable  $L_2$  counterpart does not exist, a property attributed to the lack of coherency ([Jorba-Cuscó et al., 2018](#); [Rosales et al., 2023](#)). Lastly, the analogs for  $L_2$  within the HFEM are investigated in detail by [Lian et al. \(2013\)](#), where the frequency domain information is included to characterize the fundamental frequencies associated with the HFEM analog behavior. They demonstrate that the spectrum for the  $\hat{x}$ -direction position oscillation incorporates  $3\nu_2$  as the most dominant frequency, an odd multiple of the synodic frequency. Recall from Section 3.4 that such frequency is modeled within the QBCP, but not within the HR4BP due to the doubly symmetric nature of the model resulting from the Hill approximation.

In addition to the previous contributions, it is confirmed that the HR4BP as well as two QHR4BPs admit *fixed  $L_2$  equilibrium points* within the pulsating-rotating frame. To demonstrate this behavior, Eq. (38) is recalled, corresponding to the simplified equations of motion for the (Q)HR4BPs within the pulsating-rotating frame,

$$\begin{aligned} \ddot{\vec{\rho}} = \ddot{\vec{\rho}}_{CR3BP} + \begin{bmatrix} b_4 & b_5 - 2 & 0 \\ -b_5 + 2 & b_4 & b_6 \\ 0 & -b_6 & b_4 \end{bmatrix} \dot{\vec{\rho}} + \frac{3\mu_S}{\rho_S^5} \begin{bmatrix} 0 & 2x_S y_S & 0 \\ 0 & y_S^2 - x_S^2 & y_S z_S \\ 0 & y_S z_S & \rho_S^2 + z_S^2 \end{bmatrix} \vec{\rho} \\ + \begin{bmatrix} 0 & 0 & 0 \\ 0 & b_{12} - b_{12a} & b_{11} \\ 0 & -b_{11} & b_{12} \end{bmatrix} \vec{\rho}. \end{aligned} \quad (43)$$

Any collinear Lagrange point is associated with  $\vec{\rho} = x_{eq}\hat{x}$ ,  $\dot{\vec{\rho}} = \vec{0}$ . Insert this state into Eq. (43) to result in zero acceleration, noting that  $\ddot{\vec{\rho}}_{CR3BP}$  supplies zero acceleration at the Lagrange points. The simplified expression is equivalent to the general equations as described in Eq. (36) and, thus, the HR4BP admits equilibrium points for all points  $L_{1-3}$ . Note that the formulation admits any particular solutions from the HR3BP to represent the lunar motion. Therefore, the two QHR4BPs also supply fixed  $L_{1-3}$  points. This analytical finding is confirmed with numerical tests for the HR4BP, I-QHR4BP as well as O-QHR4BP models.

The  $L_2$  counterpart behavior in various models are visually illustrated in Fig. 14. The plots correspond to the  $\hat{x} - \hat{y}$  projection of the counterparts within the pulsating-rotating frame. Note that the red square denotes the fixed  $L_2$  point. This fixed  $L_2$  behavior is observed within the CR3BP, ER3BP, HR4BP, I-QHR4BP, and O-QHR4BP. In comparison, the  $L_2$  counterpart PO within the QBCP and the complex quasi-periodic behavior within the HFEM are also plotted. In general, besides the BCR4BP, all the intermediate models investigated here supply some counterpart



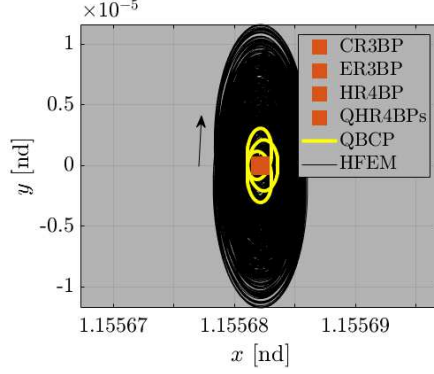


**Fig. 14:**  $L_2$  Counterparts within the pulsating-rotating frame

behaviors for the  $L_2$ . It is noteworthy, however, that the quasi-periodic behavior as observed in the HFEM is partially approximated only within the QBCP. This behavior is attributed to the peculiar nature of the equilibrium points with extremely low acceleration magnitudes in general, where the linearly approximated accelerations (via the Hill approximation, Eqs. (16), (43)) are zeros; then, higher-order accelerations govern the dynamics that are otherwise smaller than the lower-order terms. As discussed previously, the (Q)HR4BPs do not differentiate  $\theta_S$  from  $\theta_S + \pi$  due to the Hill approximation; as indicated from the QBCP and the frequency structure in the HFEM (Lian et al., 2013), the small difference between the two system configurations is one of the sources for the perturbed the  $L_2$  Lagrange point analog within the HFEM. Such behavior likely does not extrapolate to other regions within cislunar space, where the acceleration magnitudes within the pulsating-rotating frame are relatively larger in general. In such regions, the dominant frequency structures within the HFEM typically include the even multiples of  $\nu_2$ , e.g.,  $2\nu_2$  (Lian et al., 2013; Park and Howell, 2023) and the QBCP and HR4BP behave qualitatively similarly. Nonetheless, the  $L_2$  Lagrange point serves as an interesting case where the difference between the QBCP and HR4BP is most notable. This specific case highlights the nuances in constructing the model hierarchy within cislunar space; desired intermediate steps within the hierarchy indeed vary depending on the specific region of interest. Exactly at the  $L_2$  equilibrium point, although QHR4BPs contain two frequencies ( $\nu_{1,2}$  or  $\nu_{2,3}$ ) at the same time, they cannot supply the information observed in the QBCP that only models one frequency ( $\nu_2$ ). Thus, a caution is required in constructing the hierarchy within cislunar space where blindly incorporating more frequencies does not automatically lead to “higher-fidelity.” The schematic in Fig. 1 merely illustrates a general hierarchy, where desired paths to the HFEM indeed depend on specific dynamical regimes.

### 5.3 9 : 2 Synodic Resonant Halo Orbit

Future space exploration efforts include the NASA Gateway mission that leverages the Earth-Moon 9 : 2 synodic  $L_2$  halo PO. The spacecraft completes 9 revolutions per

2 synodic months, offering favorable eclipse as well as stability properties (Zimovan-Spreen et al., 2020, 2023). While previous works demonstrate a successful numerical procedure to directly transition the CR3BP periodic 9:2 halo orbit to a HFEM counterpart, leveraging intermediate models and constructing Hamiltonian structures within these models provide invaluable insights regarding the epoch dependencies of the particular solution within the HFEM. Then, insights from the intermediate models are applicable in multiple scenarios, including (1) a smoother transition process for generating a reference solution, (2) the design of control strategies to mitigate perturbations, and (3) characterization of the relative motion with respect to the Gateway mission trajectory.

The CR3BP synodic 9:2  $L_2$  halo orbit is evolved on to the counterparts within various dynamical models for illustration. The original structure in Fig. 15(a) appears within the pulsating-rotating frame. The arrow in the figure illustrates the orbit direction that remains consistent within other dynamical models. The HR4BP counterpart is plotted in Fig. 15(b). Note that the HR4BP allows a PO counterpart as the orbit satisfies the resonance condition between  $\nu_C$  and  $\nu_2$ , i.e.,  $\nu_C : \nu_2 = 9:2$ . At least two such PO counterparts exist that satisfy the perpendicular crossing condition (Sanaga and Howell, 2024); for  $\theta_S = 0$ , the spacecraft is located at the apolune or perilune along the halo orbit. For brevity, the current investigation focuses only on the apolune counterpart, corresponding to the trajectory within Fig. 15(b). Leveraging the HR4BP PO as the initial guess, the 2D-QPOs for the I-QHR4BP and O-QHR4BP are generated through the continuation process detailed in Section 5.1. The corresponding QPOs are plotted in Figs. 16(a) and 16(b) for the I-QHR4BP and O-QHR4BP, respectively. In addition to  $\nu_C = 9\nu_2/2$ , the structures also evolve with  $\nu_1$  or  $\nu_3$ . Figure 17 illustrates the counterparts within the rest of the models. The HFEM 9:2  $L_2$  halo orbit analog is constructed leveraging the initial guess provided by the CR3BP. A process similar to that in Zimovan-Spreen et al. (2023) is leveraged, using a multiple shooter to produce the trajectory within the HFEM. Twenty years of the CR3BP orbits are *stacked*, and the numerical procedure locates a nearby continuous trajectory within the HFEM. To enforce the same epoch configuration with the HR4BP, the initial epoch is selected such that the spacecraft is located at the apolune when  $\theta_S = 0$ . Such a configuration corresponds to the nearly eclipse-free phasing as discussed in Zimovan-Spreen et al. (2023). Note that the current reference Gateway trajectory in Zimovan-Spreen et al. (2023) includes additional perturbations such as the lunar harmonics as well as the solar radiation pressure; the analog solution from the current work generated with point-mass Earth-Moon-Sun HFEM may indicate some discrepancies. The HFEM analog is plotted in Fig. 17(a) within the pulsating-rotating frame. The BCR4BP counterpart is recorded by Boudad et al. (2020), where the CR3BP 9:2 NRHO numerically results in multiple counterpart POs in the BCR4BP. One such example that satisfies the phasing requirement (apolune when  $\theta_S = 0$ ) is illustrated in Fig. 17(b). The ER3BP counterpart is computed utilizing the algorithm detailed within Park and Howell (2023), where the PO from the CR3BP results in a QPO within the ER3BP at the eccentricity value of  $e = 0.055$ . The ER3BP incorporates



the  $\nu_E$  frequency that is generally close to, but not exactly,  $\nu_1$ . The QBCP PO counterpart is produced and visualized in Fig. 17(c). While potentially many counterparts exist, one with the consistent epoch requirement (apolune when  $\theta_S = 0$ ) is selected.

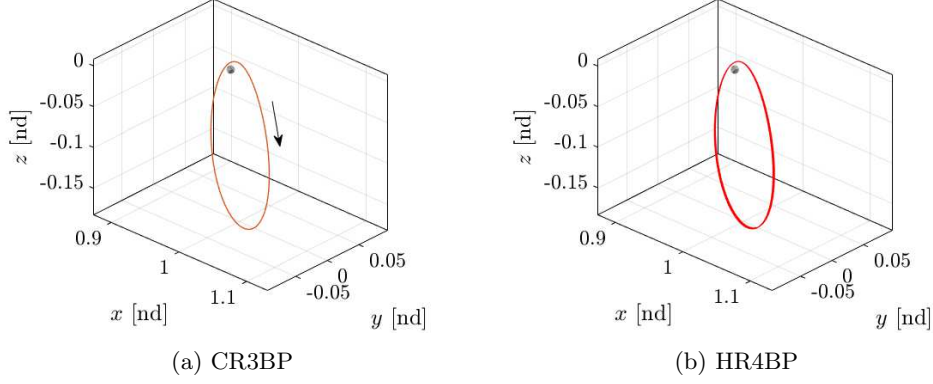


**Fig. 15:** CR3BP and HR4BP's 9:2  $L_2$  halo PO

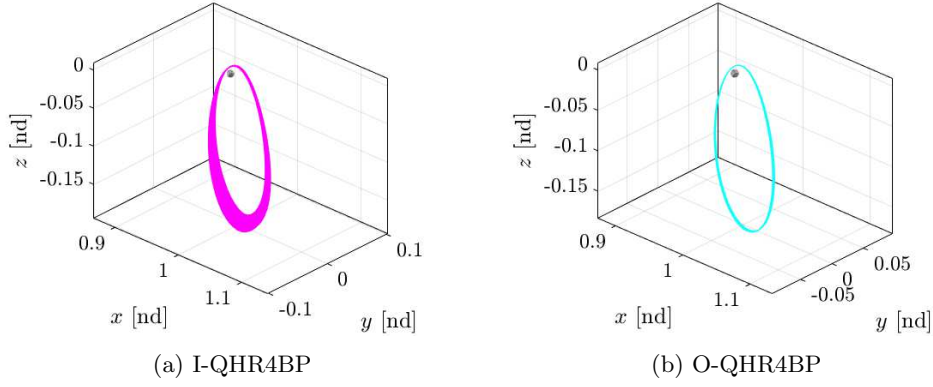
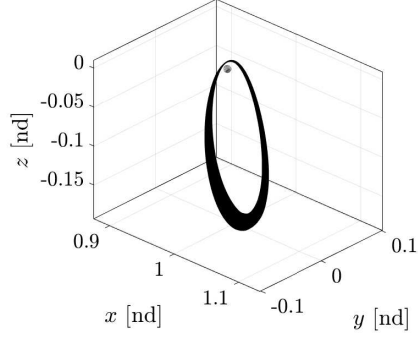
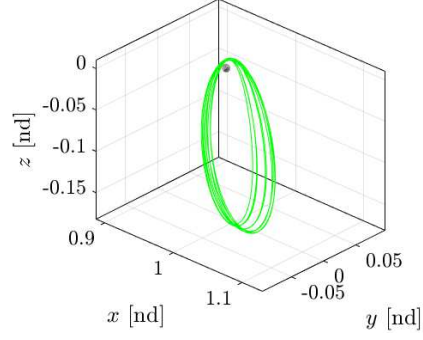


**Fig. 16:** QHR4BP's 9:2  $L_2$  halo QPO

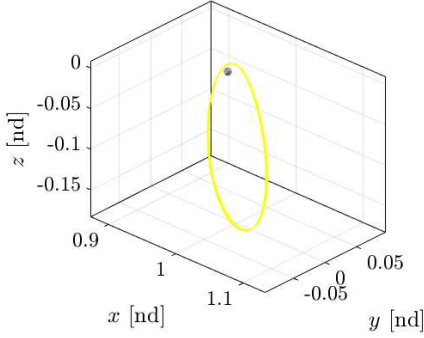
The counterparts within diverse models are compared in terms of geometry as it appears within the pulsating-rotating frame. Visually, the overall structures are maintained across all the models in configuration space. Note that the QBCP, HR4BP, and O-QHR4BP models display small deviations from the original CR3BP geometry. The structures from ER3BP and I-QHR4BP demonstrate significantly more deviations that seem to better approximate the behaviors as observed in the HFEM. The



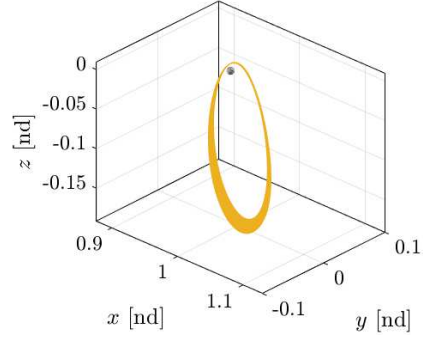
(a) HFEM, recreated from [Zimovan-Spreen et al. \(2023\)](#)



(b) BCR4BP, recreated from [Boudad et al. \(2020\)](#)



(c) QBCP



(d) ER3BP, recreated from [Park and Howell \(2024b\)](#)

**Fig. 17:** Various models deliver 9:2  $L_2$  halo counterparts

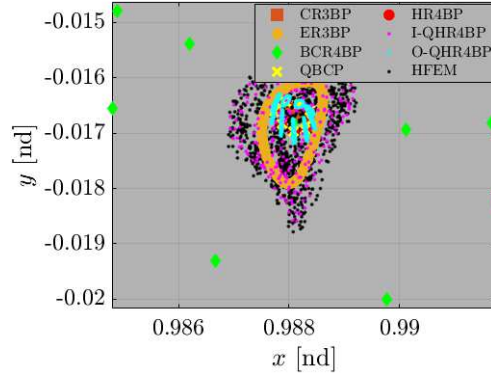
BCR4BP analog displays a qualitatively different behavior from the rest of the dynamical models. For a more clearer representation of the differences between the models, a hyperplane is constructed at  $z = 0$  on the  $\dot{z} > 0$  side, marking the position crossings along each counterpart in Fig. 18. It is first notable from Fig. 18(a) that the BCR4BP significantly deviates from the CR3BP geometry and does not seem to be located *in between* the CR3BP and HFEM structures, a property likely induced from the lack of coherency. Zoomed-in views are provided in Figs. 18(b) and 18(c). It is obvious that the major deviations within configuration space result from  $\nu_1$ , illustrated by the ER3BP, I-QHR4BP, and HFEM that all incorporate  $\nu_1$ , or  $\nu_E$  for the case in the ER3BP. This observation is also in agreement with the analyses in [Park and Howell \(2024a,b\)](#), where  $\nu_1$  is expected to dominate over  $\nu_2$  in terms of the associated perturbation magnitudes along the  $L_2$  halo orbits. To confirm, the models that do not incorporate  $\nu_1$  result in relatively smaller deviations in configuration space. These models include QBCP, HR4BP, as well as O-QHR4BP. Note that the QBCP and the

HR4BP display very similar qualitative behaviors in Fig. 18(c) that is expected from the similarity of the coefficients in both models as demonstrated from Fig. 3. Nine different crossings occur from the QBCP and the HR4BP POs by completing nine revolutions around the Moon over two synodic months. Then, the crossings along the O-QHR4BP QPO are located in nine groups (cyan dots) in the vicinity of the crossings resulting from QBCP and HR4BP POs. From the size of the deviations along the O-QHR4BP QPO with respect to the HR4BP PO, the influence from the  $\nu_3$  is likely smaller than  $\nu_2$ . Thus, for this specific dynamical regime, the perturbations in approximating the gravitational environment within the HFEM evolve in the order of  $\nu_1 > \nu_2 > \nu_3$ , viewed within the pulsating-rotating frame. Comparing the crossings from the ER3BP and I-QHR4BP, it is also true that incorporating  $\nu_2$  in addition to the  $\nu_1$  helps approximate the gravitational environment for the HFEM and predicts the evolution of the 9:2 halo counterpart. The behaviors for the I-QHR4BP and HFEM are compared in depth within Fig. 19. Different colors denote each subsequent return to the hyperplane. For example, the purple color denotes every  $(9n + 4)$ -th return to the hyperplane. The behavior for the I-QHR4BP (Fig. 19(a)) indeed demonstrates a quasi-periodic nature, where the returns to the hyperplane remain indefinitely on the closed curves. Each of the nine groups of crossings are also comparable to the crossings from the ER3BP QPO in Fig. 18(b), colored in orange. Thus, the overall shape and magnitude of the deviation is governed by the  $\nu_1$  frequency, and  $\nu_2$  perturbations place the crossings at nine different locations. This behavior is analogous to O-QHR4BP vs. HR4BP as apparent from Fig. 18(c). It is noteworthy that the color characteristics from Fig. 19(a) are quite similar to those apparent from the HFEM counterparts (Fig. 19(b)) plotted over 20 years. Thus, via incorporating two frequencies  $\nu_{1,2}$  simultaneously, the I-QHR4BP excels in approximating the HFEM behavior for the 9:2 synodic resonant halo orbit, serving as a suitable “next step” within the model hierarchy as compared to various periodically perturbed models for this specific dynamical regime.

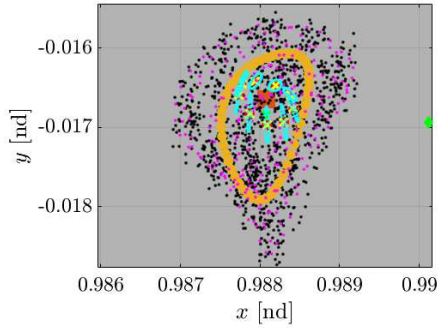
## 6 Concluding Remarks

A frequency-based hierarchy in dynamical models, within the context of the Earth-Moon multi-body dynamical regime, is investigated. Leveraging a common pulsating-rotating frame for reference, different dynamical models are represented in a consistent manner. The hierarchy between the Circular Restricted Three-Body Problem (CR3BP) and Higher-Fidelity Ephemeris Model (HFEM) is constructed by considering distinct frequency information. In general, the HFEM dynamics are represented by the coefficients,  $b_{1-13}$ , that evolve in a quasi-periodic manner under multiple frequencies. Then, different intermediate models are identified as periodically forced models that incorporate a single frequency in addition to the CR3BP, and quasi-periodically force models that incorporate two different frequencies at the same time.

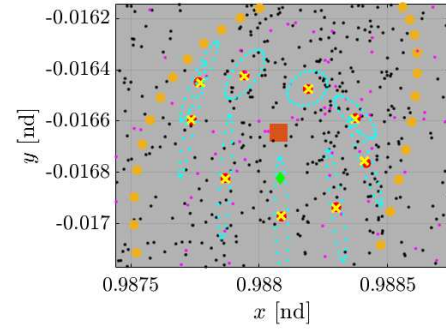
The nature of coherent solar gravity modeling is analyzed in terms of the coefficients,  $b_{1-13}$ . It is observed that analytical cancellations occur for dynamical models that introduce solar gravity in a coherent manner; such behavior results in nearly linear acceleration patterns within the common pulsating-rotating frame. Then, two coherent periodically perturbed four-body problems, the Quasi Bi-Circular Problem



(a) Zoomed-out view

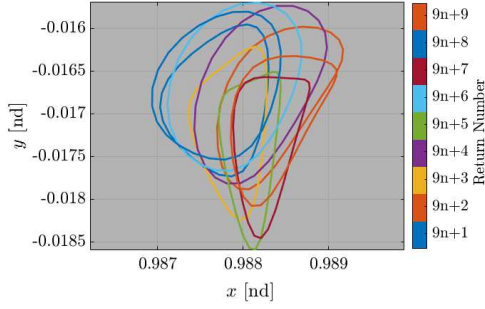


(b) Zoomed-in view

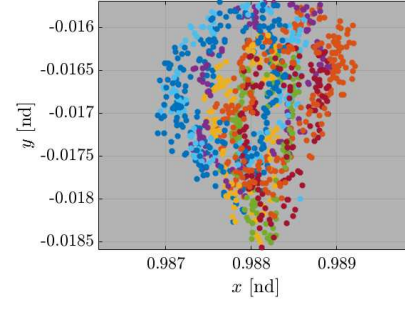


(c) Zoomed-in view 2

**Fig. 18:** Comparison of  $L_2$  9:2 halo counterparts from different models at the hyper-plane ( $z = 0, \dot{z} > 0$ )



(a) I-QHR4BP



(b) HFEM

**Fig. 19:** Crossings for the I-QHR4BP and HFEM 9:2  $L_2$  halo counterparts

(QBCP) and the Hill Restricted Four-Body Problem (HR4BP), are investigated within the common formulation, extending the existing catalog for the periodically forced models within the hierarchy of models. The coefficients for QBCP and HR4BP are compared to each other and to the HFEM. A global similarity for the two four-body problems is confirmed. It is also observed that these two models generally face challenges in approximating the HFEM behavior that mainly originates from frequencies associated with the anomalistic and draconic lunar months.

To complement the hierarchy of models, two coherent quasi-periodically perturbed models are designed, denoted the Quasi-Hill Restricted Four-Body Problem (QHR4BP). The insights from Hill’s lunar theory and the Hill Restricted Three-Body Problem (HR3BP) are leveraged. The linear stability structure for the lunar variation Periodic Orbit (PO) are investigated, leading to two families of nonlinear Quasi-Periodic Orbits (QPOs) that increase the eccentricity and inclination values for the lunar motion. These HR3BP QPOs are leveraged to supply QHR4BPs. The quasi-periodically perturbed models are investigated in terms of the coefficients within the pulsating-rotating frame, demonstrating capabilities in better approximating the HFEM dynamics.

The capabilities of various dynamical models are investigated for two sample scenarios within the Earth-Moon system, shedding light on the model hierarchy. First, the  $L_2$  Lagrange point and its counterparts within various models are investigated. It is demonstrated that multiple models produce equilibrium counterparts even in the presence of time-dependent perturbations, with only the QBCP partially succeeding in estimating the complex behavior within the HFEM. Secondly, the 9 : 2 halo PO’s counterparts are investigated. By comparing the geometries within the pulsating-rotating frame, the most dominant perturbations are shown to be generally associated with the following order: (1) Earth-Moon “eccentricity”, (2) in-plane solar gravity, and (3) out-of-plane solar gravity. The QHR4BP that incorporates the first two types of perturbations thus serves as a suitable quasi-periodically perturbed model for the specific scenario.

**Acknowledgements.** Valuable discussions with members from Multi-Body Dynamics Research Group are appreciated. Beom Park would like to thank Kwanjeong Educational Foundation for the financial support. Rohith Reddy Sanaga would like to thank Department of Computer Science Department at Purdue University. Portions of this work are also supported by Purdue University and under Grant NASA JSC 80NSSC18M0122.

## Appendix A Review of the QBCP Expressions from Andreu (1998)

The expressions that appear in the original derivation of the QBCP from Andreu (1998) are reviewed. A group of coefficients,  $\alpha_k$ ,  $1 \leq k \leq 8$ , appear with the following physical interpretations,

$$\alpha_1 = \frac{l_*^2}{l^2}, \quad \alpha_1^* = -\frac{2l_*^2 l'}{l^3 t_*'}, \quad \alpha_2 = -\frac{l'}{l t_*'}, \quad \alpha_2^* = \frac{-l'' l + l'^2}{l^2 t_*'^2}$$

$$\begin{aligned}
\alpha_3 &= \frac{h}{l^2 t_*'}, \quad \alpha_3^* = \frac{h'l - 2hl'}{l^3 t_*'^2} \\
\alpha_4 &= -\frac{1}{l_*'^2 t_*'^2} \vec{R}_{EM} \cdot \vec{B}''', \quad \alpha_5 = -\frac{1}{l_*'^2 t_*'^2} \vec{R}_{EM} \times \vec{B}''', \quad \alpha_6 = \frac{l_*}{l} \\
\alpha_7 &= \frac{\mu_S + 1}{\mu_S} \frac{\vec{R}_{EM} \cdot \vec{B}}{l^2} = -x_S, \quad \alpha_8 = \frac{\mu_S + 1}{\mu_S} \frac{\vec{R}_{EM} \times \vec{B}}{l^2} = -y_S.
\end{aligned} \tag{A1}$$

The  $\alpha_k$  functions are assumed in the following forms,

$$\begin{aligned}
\alpha_k &= \sum_j \alpha_{kj} \cos(jt_*), & k &= 1, 3, 4, 6, 7 \\
\alpha_k &= \sum_j \alpha_{kj} \sin(jt_*), & k &= 2, 5, 8,
\end{aligned} \tag{A2}$$

where sines and cosines coefficients  $\alpha_{kj}$  are included in Tables A1-A3. Note that some numbers appear with opposite signs compared to Andreu (1998) due to the coordinate change.

**Table A1:** Coefficients for the QBCP:  $\alpha_{1j}, \alpha_{2j}, \alpha_{3j}$ , recreated from Andreu (1998)

$j$	$\alpha_{1j}$	$\alpha_{2j}$	$\alpha_{3j}$
0	1.00184160892484e+0	0	9.99999999999999e-1
1	-5.76751772619840e-4	2.64437602849994e-4	-5.63412599755369e-4
2	1.43877702550763e-2	-1.32868690340017e-2	1.88968744017288e-2
3	2.63036297497202e-6	-9.38609320808975e-6	9.91175880256713e-6
4	1.17627835611893e-4	-1.21850905751741e-4	1.56870813603113e-4
5	8.06858139100555e-8	-1.52212759855701e-7	1.70776257617348e-7
6	9.84324976650129e-7	-1.07210266427800e-6	1.31961367970744e-6
7	1.17205439441820e-9	-1.88937126137405e-9	2.13655004198565e-9
8	8.31190597087959e-9	-9.32498503892749e-9	1.11716891667389e-8
9	1.40858423869539e-11	-2.11449098128026e-11	2.38725363103111e-11
10	7.05071378646684e-11	-8.07111174314435e-11	9.49087962209590e-11
11	1.49425963491046e-13	-2.21811805042017e-13	2.46273258155843e-13
12	5.98241897945123e-13	-7.03615516188201e-13	8.10106770800974e-13
14		-3.96722989612218e-15	1.35423199846983e-15

## Appendix B 2D-QPO Computation Algorithm

While multiple numerical schemes exist to approximate the QPO structures, an algorithm designed by algorithm developed by Gómez and Mondelo (2001) as well as Olikara and Scheeres (2012) (GMOS) is leveraged. Other related references include Olikara and Howell (2010); Olikara et al. (2016); Baresi et al. (2018); McCarthy and Howell (2021). The GMOS algorithm formulates a targeting problem to numerically compute a 2D QPO by leveraging a stroboscopic map with the period corresponding

**Table A2:** Coefficients for the QBCP:  $\alpha_{4j}, \alpha_{5j}, \alpha_{6j}$ , recreated from Andreu (1998)

$j$	$\alpha_{4j}$	$\alpha_{5j}$	$\alpha_{6j}$
0	-9.75524232748489e-4	0	1.00090745770816e+00
1	-2.15476436270711e+0	2.19257075104007e+00	-2.87092175005313e-4
2	3.65748446896870e-4	-3.33721048547287e-4	7.18717799861288e-3
3	-3.29567337616659e-3	3.29500143020097e-3	2.35118314721325e-6
4	3.30103140081243e-7	-3.10063505305263e-7	4.58575897112206e-5
5	-1.27884068737632e-5	1.2777733685413e-5	3.84868362010704e-8
6	-2.62379795212793e-9	2.65280640549811e-9	3.27067750493567e-7
7	-6.53380551456151e-8	6.52847924508507e-8	4.40696648104188e-10
8	-3.89172070778351e-11	3.89172070778351e-11	2.45260066257026e-9
9	-3.81227583894443e-10	3.81227583894443e-10	4.54293880067344e-12
10	-3.90790604983488e-13	3.90790604983488e-13	1.89234885511262e-11
11	-2.40747118757644e-12	2.40747118757644e-12	4.17842010148012e-14
12	0	0	1.48004894696158e-13

**Table A3:** Coefficients for the QBCP:  $\alpha_{7j}, \alpha_{8j}$ , recreated from Andreu (1998)

$j$	$\alpha_{7j}$	$\alpha_{8j}$
0	-6.31406956800623e-2	0
1	-3.88563862309805e+2	3.89743725623765e+02
2	1.73691020334556e-1	-1.73427916632252e-1
3	-3.38290807166970e+00	3.38569648664212e+00
4	1.57483756538049e-4	-1.55588663241340e-4
5	-2.93636048900444e-2	2.93758267196753e-2
6	-1.22443455011601e-5	1.22585121310793e-5
7	-2.53893543426244e-4	2.53959688769264e-4
8	-2.27892904000757e-7	2.28002922020236e-7
9	-2.19043270618166e-6	2.19083462442904e-6
10	-3.03331196123435e-9	3.03610903512086e-9
11	-1.88697154529022e-8	1.88745764757932e-8
12	-3.43237510689845e-11	3.43237510689845e-11
13	-1.61151370399910e-10	1.63172364150645e-10

to one of the frequencies. While either the latitudinal frequency,  $\nu_{lat}$ , or the longitudinal frequency,  $\nu_{lon}$ , may be utilized,  $\nu_{lon}$  is selected for a consistent analysis in the current investigation. Then, at the stroboscopic map, the 2D-QPO now appears as an invariant curve, governed by the latitudinal angle,  $\theta_{lat}$ . Denoting the invariant curve as  $\vec{u} = \vec{u}(\theta_{lat})$ , the Discrete Fourier Transform (DFT) is leveraged to numerically approximate the smooth invariant curve with finite sample points. Thus,

$$\vec{u}(\theta_{lat}) \approx \sum_{k=0}^{N-1} \vec{D}_k e^{(j\theta_{lat}k)}, \quad (\text{B3})$$

where  $N$  is the number of sample points, assumed to be 25 in the current investigation and  $j = \sqrt{-1}$ . The Fourier coefficients are denoted as  $\vec{D}$ . The  $N$  selected points along the invariant curve are propagated for one stroboscopic mapping time, i.e., the

longitudinal period. The end state is denoted as  $\vec{\Psi}(\vec{u}(\theta_k))$ ,  $1 \leq k \leq N$ , where  $\vec{\Psi}$  is the stroboscopic mapping function under a selected dynamical model. These end states are also on the invariant curve but rotate by  $\sigma$ , the rotation number. Thus,

$$\vec{\Psi}(\vec{u}(\theta_{lat})) = \vec{u}(\theta_{lat} + \sigma), \quad (\text{B4})$$

resulting in the *invariance condition*. This condition is leveraged to formulate a numerical targeting problem that solves for 2D-QPOs.

## Appendix C Eccentricity from Hill's Lunar Theory

From Darwin (2009/1916), in the vicinity of the lunar variational PO, the linear approximation for the in-plane invariant curve constructed at  $\theta_2 = 0$  is expressed in terms of the approximate eccentricity,  $e_a$ , as follows,

$$\xi(\theta_2 = 0) \approx A_0 \left( 1 - m^2 - \frac{15}{8} m e_a \cos(\theta_1) - e_a \cos(\theta_1) \right) \quad (\text{C5})$$

$$\eta(\theta_2 = 0) \approx A_0 \left( -\frac{15}{4} m e_a \sin(\theta_1) + 2 e_a \sin(\theta_1) \right), \quad (\text{C6})$$

where  $A_0 = a_0(1 - m^2/6)$  leveraging  $a_0$  from Eq. (5). Note that the out-of-plane component,  $\zeta$ , remains zero. Also,  $\theta_1 = 0, \pi$  leads to  $\eta = 0$ , or, the crossings of the invariant curve at the  $\hat{i}_H$ -axis within the Hill frame. At these two locations, the  $\xi$  values along the invariant curve are minimized and maximized, respectively. Thus,

$$\xi_{max,min}(\theta_2 = 0) = A_0(1 - m^2 \pm \frac{15}{8} m e_a \pm e_a). \quad (\text{C7})$$

This equation straightforwardly leads to Eq. (41).

## Appendix D Inclination from Hill's Lunar Theory

From Darwin (2009/1916), the linear approximation for the out-of-plane invariant curve ( $\theta_{lon} = 0$ ) is expressed with a quantity  $B_0 := A_0 \tan i_a$ , where  $i_a$  is the approximate inclination of the lunar orbit with respect to the ecliptic plane. The expression leads to,

$$\zeta \approx B_0 \left( \cos(\theta_3) - \frac{3}{8} m \cos(\theta_3) \right). \quad (\text{D8})$$

The linear variation for the other two directions, i.e.,  $\hat{i}_H, \hat{j}_H$ , remains zero. Then, trivially,

$$\zeta_{max,min}(\theta_2 = 0) = B_0(1 \mp \frac{3}{8} m), \quad (\text{D9})$$

leading to Eq. (42).



## References

- Andreu, M. (1998) The Quasi-bicircular Problem. PhD dissertation, Universitat de Barcelona, Spain
- Assadian, N., Pourtakdoust, S.H. (2010) On the quasi-equilibria of the BiElliptic four-body problem with non-coplanar motion of primaries. *Acta Astronautica* 66(1):45–58. <https://doi.org/10.1016/j.actaastro.2009.05.014>
- Aydin, C. (2023) From Babylonian lunar observations to Floquet multipliers and Conley–Zehnder indices. *Journal of Mathematical Physics* 64(8):082,902. <https://doi.org/10.1063/5.0156959>
- Baresi, N., Olikara, Z.P., Scheeres, D.J. (2018) Fully Numerical Methods for Continuing Families of Quasi-Periodic Invariant Tori in Astrodynamics. *The Journal of the astronautical sciences* 65:157–182. <https://doi.org/10.1007/s40295-017-0124-6>
- Beutler, G. (2004) *Methods of Celestial Mechanics: Volume II: Application to Planetary System, Geodynamics and Satellite Geodesy*. Springer Science & Business Media, <https://doi.org/10.1007/b137725>
- Boudad, K.K., Howell, K.C., Davis, D.C. (2020) Dynamics of synodic resonant near rectilinear halo orbits in the bicircular four-body problem. *Advances in Space Research* 66(9):2194–2214. <https://doi.org/10.1016/j.asr.2020.07.044>
- Brown, E.W. (1896) *An Introductory Treatise on the Lunar Theory*. The Cambridge University Press
- Brown, G.M., Peterson, L.T., Henry, D.B., et al. (2024) Structure of periodic orbit families in the hill restricted 4-body problem. arXiv preprint arXiv:240219181 <https://doi.org/10.48550/arXiv.2402.19181>
- Darwin, G.H. (2009/1916) *The Scientific Papers of Sir George Darwin: Supplementary Volume*. Cambridge Library Collection - Physical Sciences, Cambridge University Press (Original work published in 1916), <https://doi.org/10.1017/CBO9780511703515>
- Dei Tos, D.A. (2014) Automated Trajectory Refinement of Three-Body Orbits in the Real Solar System Model. Master’s thesis, Politecnico di Milano, Italy, <https://doi.org/10.13140/RG.2.2.11084.82561>
- Dei Tos, D.A., Topputo, F. (2017) On the advantages of exploiting the hierarchical structure of astrodynamical models. *Acta Astronautica* 136:236–247. <https://doi.org/10.1016/j.actaastro.2017.02.025>
- Ferrari, F., Lavagna, M. (2018) Periodic motion around libration points in the elliptic restricted three-body problem. *Nonlinear Dynamics* 93:453–462. <https://doi.org/10.1007/s11071-018-0453-4>

- Gao, C., Masdemont, J.J., Gómez, G., et al. (2022) The web of resonant periodic orbits in the Earth–Moon Quasi-Bicircular Problem including solar radiation pressure. *Communications in Nonlinear Science and Numerical Simulation* 111:106,480. <https://doi.org/10.1016/j.cnsns.2022.106480>
- Gómez, G., Masdemont, J.J., Mondelo, J.M. (2002) Solar system models with a selected set of frequencies. *Astronomy & Astrophysics* 390(2):733–749. <https://doi.org/10.1051/0004-6361:20020625>
- Gutzwiller, M.C. (1998) Moon–Earth–Sun: The oldest three-body problem. *Reviews of Modern Physics* 70(2):589–639. <https://doi.org/10.1103/RevModPhys.70.589>
- Gómez, G., Mondelo, J. (2001) The dynamics around the collinear equilibrium points of the rtbp. *Physica D: Nonlinear Phenomena* 157(4):283–321. [https://doi.org/10.1016/S0167-2789\(01\)00312-8](https://doi.org/10.1016/S0167-2789(01)00312-8)
- Hénon, M. (1969) Numerical exploration of the restricted problem, v. *Astronomy and Astrophysics*, vol 1, p 223–238 (1969) 1:223–238. URL <https://ui.adsabs.harvard.edu/abs/1969A&A.....1..223H>
- Henry, D.B., Rosales, J.J., Brown, G.M., et al. (2023) Quasi-periodic orbits around Earth–Moon  $L_1$  and  $L_2$  in the Hill restricted four-body problem. In: AAS/AIAA Astrodynamics Specialist Conference, Big Sky, Montana, August 13–17, 2023.
- Hill, G.W. (1878) Researches in the lunar theory. *American journal of Mathematics* 1(3):245–260. <https://doi.org/10.2307/2369313>
- Jorba, À., Villanueva, J. (1997) On the persistence of lower dimensional invariant tori under quasi-periodic perturbations. *Journal of Nonlinear Science* 7(5):427–473. <https://doi.org/10.1007/s003329900036>
- Jorba-Cuscó, M., Farrés, A., Jorba, À. (2018) Two periodic models for the Earth–Moon system. *Frontiers in Applied Mathematics and Statistics* 4:32. <https://doi.org/10.3389/fams.2018.00032>
- Kelly, P., Junkins, J.L., Majji, M. (2023) Resonant quasi-periodic orbits in the bi-elliptic restricted four-body problem. In: AAS/AIAA Astrodynamics Specialist Conference, Big Sky, Montana, August 13–17, 2023.
- Lian, Y., Gómez, G., Masdemont, J.J., et al. (2013) A note on the dynamics around the lagrange collinear points of the earth–moon system in a complete solar system model. *Celestial Mechanics and Dynamical Astronomy* 115:185–211. <https://doi.org/10.1007/s10569-012-9459-2>

- McCarthy, B.P., Howell, K.C. (2021) Leveraging quasi-periodic orbits for trajectory design in cislunar space. *Astrodynamics* 5(2):139–165. <https://doi.org/10.1007/s42064-022-0136-2>
- Meyer, K.R., Offin, D.C. (2018) Introduction to hamiltonian dynamical systems and the N-body problem. Springer International Publishing, <https://doi.org/10.1007/978-1-4757-4073-8>
- Mohn, L., Kevorkin, J. (1967) Some limiting cases of the restricted four-body problem. *Astronomical Journal* 72(8):959–963. <https://doi.org/10.1086/110370>
- Olikara, Z.P., Howell, K.C. (2010) Computation of quasi-periodic invariant tori in the restricted three-body problem. In: 20th AAS/AIAA Space Flight Mechanics Meeting, San Diego, California
- Olikara, Z.P., Scheeres, D.J. (2012) Numerical method for computing quasi-periodic orbits and their stability in the restricted three-body problem. *Advances in the Astronautical Sciences* 145(911-930):911–930
- Olikara, Z.P., Scheeres, D.J. (2017) Mapping connections between planar sun-earth-moon libration orbits. In: 27th AAS/AIAA Space Flight Mechanics Meeting, American Astronautical Society San Antonio, Texas
- Olikara, Z.P., Gómez, G., Masdemont, J.J. (2016) A Note on Dynamics About the Coherent Sun–Earth–Moon Collinear Libration Points. In: *Astrodynamics Network AstroNet-II*. Springer International Publishing, pp 183–192, [https://doi.org/10.1007/978-3-319-23986-6\\_13](https://doi.org/10.1007/978-3-319-23986-6_13)
- Park, B., Howell, K. (2024a) Characterizing transition-challenging regions leveraging the elliptic restricted three-body problem: L2 halo orbits. In: *AIAA SCITECH 2024 Forum*, <https://doi.org/10.2514/6.2024-1455>
- Park, B., Howell, K.C. (2023) Leveraging the elliptic restricted three-body problem for characterization of multi-year earth-moon  $L_2$  halos in an ephemeris model. In: *AAS/AIAA Astrodynamics Specialist Conference*, Big Sky, Montana, August 13-17, 2023.
- Park, B., Howell, K.C. (2024b) Assessment of dynamical models for transitioning from the Circular Restricted Three-Body Problem to an ephemeris model with applications. *Celestial Mechanics and Dynamical Astronomy* 136(6). <https://doi.org/10.1007/s10569-023-10178-9>
- Park, R.S., Folkner, W.M., Williams, J.G., et al. (2021) The jpl planetary and lunar ephemerides de440 and de441. *The Astronomical Journal* 161(3):105. <https://doi.org/10.3847/1538-3881/abd414>

- Peng, H., Xu, S. (2015) Stability of two groups of multi-revolution elliptic halo orbits in the elliptic restricted three-body problem. *Celestial Mechanics and Dynamical Astronomy* 123(3):279–303. <https://doi.org/10.1007/s10569-015-9635-2>
- Peterson, L.T., Rosales, J.J., Scheeres, D.J. (2023) The vicinity of Earth–Moon  $L_1$  and  $L_2$  in the Hill restricted 4-body problem. *Physica D: Nonlinear Phenomena* 455:133,889. <https://doi.org/10.1016/j.physd.2023.133889>
- Rosales, J.J., Jorba, A., Jorba-Cuscó, M. (2021) Families of Halo-like invariant tori around  $L_2$  in the Earth-Moon Bicircular Problem. *Celestial Mechanics and Dynamical Astronomy* 133(4):16. <https://doi.org/10.1007/s10569-021-10012-0>
- Rosales, J.J., Jorba, À., Jorba-Cuscó, M. (2023) Invariant manifolds near  $L_1$  and  $L_2$  in the quasi-bicircular problem. *Celestial Mechanics and Dynamical Astronomy* 135(15). <https://doi.org/10.1007/s10569-023-10129-4>
- Sanaga, R.R., Howell, K. (2024) Analyzing the Challenging Region in the Earth-Moon  $L_2$  Halo Family via Hill Restricted Four-Body Problem Dynamics. In: *AIAA SCITECH 2024 Forum*, <https://doi.org/10.2514/6.2024-1451>
- Sanaga, R.R., Howell, K.C. (2023) Synodic resonant halo orbits in the Hill restricted four-body problem. In: *33rd AAS/AIAA Spaceflight Mechanics Meeting*, Austin, Texas, January 15–19, 2023.
- Scheeres, D.J. (1998) The Restricted Hill Four-Body Problem with Applications to the Earth-Moon-Sun system. *Celestial Mechanics and Dynamical Astronomy* 70:75–98. <https://doi.org/10.1023/A:1026498608950>
- Szebehely, V. (1967) *Theory of Orbit: The Restricted Problem of Three Bodies*. Academic Press, <https://doi.org/10.1016/B978-0-12-395732-0.X5001-6>
- Villegas-Pinto, D., Baresi, N., Locoche, S., et al. (2023) Resonant quasi-periodic near-rectilinear Halo orbits in the Elliptic-Circular Earth-Moon-Sun Problem. *Advances in Space Research* 71(1):336–354. <https://doi.org/10.1016/j.asr.2022.08.011>
- Wintner, A. (1947) *The analytical foundations of celestial mechanics*. Princeton University Press
- Zimovan-Spreen, E.M., Howell, K.C., Davis, D.C. (2020) Near rectilinear halo orbits and nearby higher-period dynamical structures: orbital stability and resonance properties. *Celestial Mechanics and Dynamical Astronomy* 132(5):28. <https://doi.org/10.1007/s10569-020-09968-2>
- Zimovan-Spreen, E.M., Scheuerle, S.T., McCarthy, B.P., et al. (2023) Baseline Orbit Generation for Near Rectilinear Halo Orbits. In: *AAS/AAIA Astrodynamics Specialist Conference*, Big Sky, Montana, August 13–17, 2023.